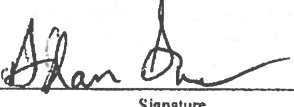

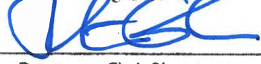


Justin G. Casaus


**An Experimental Study of The Incorporation of Sulfur In Fluorapatite During Metasomatism**

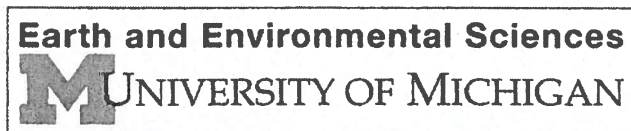
submitted in partial fulfillment of the requirements for the degree of  
**Master of Science in Earth and Environmental Sciences**  
Department of Earth and Environmental Sciences  
The University of Michigan

 Signature	Accepted by: Adam Simon Name	06/21/23 Date
 Signature	Jeffrey Alt Name	7/12/23 Date
 Department Chair Signature	Julia Cole Name	7/31/23 Date

I hereby grant the University of Michigan, its heirs and assigns, the non-exclusive right to reproduce and distribute single copies of my thesis, in whole or in part, in any format. I represent and warrant to the University of Michigan that the thesis is an original work, does not infringe or violate any rights of others, and that I make these grants as the sole owner of the rights to my thesis. I understand that I will not receive royalties for any reproduction of this thesis.

- Permission granted.  
 Permission granted to copy after: \_\_\_\_\_  
 Permission declined.

 06/21/23  
Author Signature



1 Revision 1

2 Word Count: ca. 10,389

3 **Title:** An Experimental Study of The Incorporation of Sulfur In Apatite During Metasomatism

4 Part I. Fluorapatite

5

6 **Authors:** Casaus, Justin<sup>1</sup>, Harlov, Daniel<sup>2,3,4</sup>, Konecke, A. Brian<sup>5</sup>, Simon, C. Adam<sup>1</sup>

7

8 **Affiliations:**

9 <sup>1</sup>University of Michigan, Department of Earth and Environmental Sciences, Ann Arbor,  
10 Michigan, 48109, USA

11 <sup>2</sup>Deutsches GeoForschungsZentrum-GFZ, Telegrafenberg, 14473 Potsdam, Germany

12 <sup>3</sup>Department of Geology, University of Johannesburg P.O. Box 524, Auckland Park,  
13 2006 South Africa

14 <sup>4</sup>Faculty of Earth Resources, China University of Geosciences, 430074 Wuhan, China

15 <sup>5</sup>Fathom Geophysics, LLC, Newark, Ohio, 43056, USA

16

17

### **Abstract**

18 The mineral apatite [Ca<sub>10</sub>(PO<sub>4</sub>)<sub>6</sub>(F,Cl,OH)<sub>2</sub>] is ubiquitous in terrestrial geologic systems. The  
19 apatite supergroup is capable of incorporating a significant portion of the periodic table of  
20 elements. As such, apatite is commonly used as a tool for, *inter alia*, U-Pb and fission track  
21 dating of processes in igneous and metamorphic systems, determining the water content of  
22 silicate melts at the time of apatite crystallization, and using Sr-Nd isotope systematics  
23 fingerprinting the source of magmas and possible assimilation of crustal rocks. Despite apatite

24 being ubiquitous in igneous and magmatic-hydrothermal systems, there is a dearth of data that  
25 constrain the partitioning of trace elements between apatite and aqueous hydrothermal fluids.  
26 Here, we report results from hydrothermal alteration and crystallization experiments at 800 °C  
27 and 1 GPa that constrain the partitioning of sulfur, iron, strontium, and the rare earth element  
28 (REE) cerium between fluorapatite and fluids of variable compositions. The data demonstrate  
29 that sulfur is incorporated in apatite through a balanced coupled substitution with Na and Si. The  
30 data also demonstrate that the presence of Sr in the aqueous fluid promotes the incorporation of  
31 Na and S in apatite. Our data reveal a previously unknown intrinsic relationship among Fe, Ce,  
32 and S in metasomatized fluorapatite that is explained by coupled substitutions between  $\text{Fe}^{3+}$  and  
33  $\text{Ce}^{3+}$  with  $\text{S}^{4+}$ . The concentrations of Cl, OH, and S in run-produce apatite are positively  
34 correlated with each other, which indicates that the halogen chemistry of apatite plays a  
35 determinative role in the incorporation of S in apatite. Overall, the data demonstrate that  
36 incorporation of sulfate and sulfite into apatite during metasomatism depends on the abundance  
37 of charge-balancing cations in the hydrothermal fluid.

38

39 **Keywords:** Fluorapatite, hydrothermal, sulfur, iron, strontium, rare earth element

40

41

## INTRODUCTION

42 Apatite is a common accessory mineral in sedimentary, igneous, and metamorphic rocks. The  
43 apatite supergroup crystal chemical formula is  $^{\text{IX}}\text{M1}_4^{\text{VII}}\text{M2}_6(^{\text{IV}}\text{TO}_4)_6\text{X}_2$  ( $Z = 1$ ), where the M sites  
44 are most commonly occupied by Ca, the T site by P, and the X site by F, Cl or OH. The Roman  
45 numeral superscripts indicate the ideal coordination numbers. Apatite can structurally  
46 incorporate dozens of elements including  $\text{Pb}^{2+}$ ,  $\text{Ba}^{2+}$ ,  $\text{Sr}^{2+}$ ,  $\text{Mn}^{2+}$ ,  $\text{Na}^+$ ,  $\text{Ce}^{3+}$ ,  $\text{La}^{3+}$ ,  $\text{Y}^{3+}$  and  $\text{Bi}^{3+}$  on

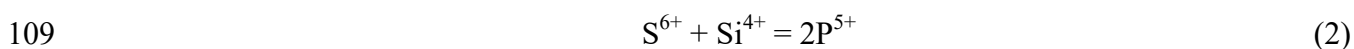
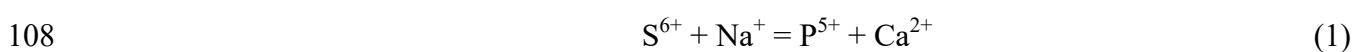
47 the M-sites, and  $\text{As}^{5+}$ ,  $\text{V}^{5+}$ ,  $\text{Si}^{4+}$ ,  $\text{S}^{6+}$  and  $\text{B}^{3+}$  on the T-site (Pasero et al., 2010; Pan and Fleet,  
48 2002). Apatite can also incorporate multiple oxidation states of sulfur, with  $\text{S}^{6+}$  and  $\text{S}^{4+}$  on the T-  
49 site and  $\text{S}^{2-}$  on the X-site (Kim et al., 2017, 2022). The incorporation of non-essential structural  
50 constituents into the M, T and X sites is dictated by pressure, temperature, redox conditions, and  
51 for igneous and hydrothermal apatite the composition of the fluid medium from which apatite  
52 grows or, in the case of metamorphic apatite, the prograde and retrograde P-T paths. A plethora  
53 of studies have documented that the abundances of elements and their isotopes in apatite that  
54 crystallized from silicate melt can provide insight into the evolution of the magmatic system  
55 provided that metasomatism and/or dissolution-reprecipitation did not occur after crystallization  
56 (Watson and Green, 1981; Zhu and Sverjensky, 1991; Pan and Fleet, 2002). For example, the  
57 concentrations of rare earth elements (REE) in apatite can be used to infer melt source, the U-Pb  
58 and Lu-Hf concentrations in apatite can be used to quantify the timing of apatite crystallization  
59 (Spear and Pyle, 2002; Chew and Spinkings, 2015), and the temperature controlled F-OH  
60 partitioning between apatite and biotite is used as a geothermometer (Sallet, 2000). Several  
61 studies have reported that the concentrations of the trace elements Sr, Mn and Y, chondrite-  
62 normalized REE patterns and Eu anomaly severity, and halogen fractionation (Br/Cl and I/Cl) in  
63 apatite are unique to specific rock types and have implications for mineral exploration  
64 (Andersson et al., 2019; Belousova et al., 2002; Mao et al., 2016; Zhou et al., 2022). Lastly, the  
65 measured abundances of  $\text{S}^{6+}$ ,  $\text{S}^{4+}$  and  $\text{S}^{2-}$ , reported as the ratio of  $\text{S}^{6+}/\Sigma\text{S}$ , in magmatic apatite can  
66 be used to quantify oxygen fugacity ( $f\text{O}_2$ ) at the time of apatite crystallization (Konecke et al.,  
67 2019). The compositions and textures of magmatic apatite have also been used to understand  
68 how fluid-induced metasomatism affects primary apatite. For example, Harlov et al. (2002b)  
69 reported that hydrothermal alteration of primary fluorapatite in samples from the Kiirunavaara

70 magnetite-apatite deposit in northern Sweden resulted in decreased concentrations of Na, S, Fe,  
71 Sr, and Ce concentrations in regions of individual grains that were metasomatized by a Cl-OH-  
72 fluid. Contrarily, Palma et al. (2019) reported that hydrothermal alteration of fluorapatite in  
73 samples from the Mina Carmen iron oxide-apatite (IOA) deposit of northern Chile resulted in an  
74 increase in the concentrations of Na, S, Fe, and Sr in regions of apatite grains that were  
75 metasomatized by a Cl-OH-S-fluid. Konecke et al. (2017) reported that the same metasomatized  
76 fluorapatite grains studied by Palma et al. (2019) contain  $S^{6+}$ ,  $S^{4+}$ , and  $S^{2-}$ , in the metasomatized  
77 regions of individual grains.

78  
79 A limited number of experimental studies have been conducted in order to better understand how  
80 the composition of apatite is affected by hydrothermal (metasomatic) alteration. Harlov et al.  
81 (2002a) experimentally reacted unaltered Ødegårdens Verk chlorapatite grains with pure H<sub>2</sub>O, a  
82 50/50 molar mix of H<sub>2</sub>O and CaF<sub>2</sub>, and CO<sub>2</sub> with 1-2 wt.% H<sub>2</sub>O at 300 – 900 °C and 0.5 – 1  
83 GPa. They report that hydrothermal alteration of the chlorapatite grains with pure H<sub>2</sub>O resulted  
84 in a depletion of Na, Si, and (Y + REE) in apatite and concomitant growth of monazite and  
85 xenotime inclusions. Those authors also reported that hydrothermal alteration of chlorapatite  
86 grains with a F-bearing fluid resulted in the enrichment of F and Si in apatite and sparse growth  
87 of monazite. Those authors reported that reaction of chlorapatite with a CO<sub>2</sub>-bearing fluid  
88 resulted in no measurable changes to the starting apatite. Harlov and Förster (2003)  
89 experimentally reacted natural light REE (LREE) enriched Durango fluorapatite grains with pure  
90 H<sub>2</sub>O, brines bearing Na, Ca, or K, and CO<sub>2</sub> bearing fluids at 300 – 900 °C and 0.5 – 1 GPa.  
91 Those authors reported increased fluorapatite reactivity with increased temperature and the  
92 leaching of the LREEs, Na, and Si from metasomatized regions of the run-product fluorapatite

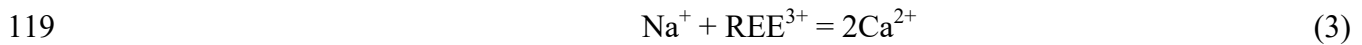
93 grains. They also reported that the increased activity of Na and Ca in the fluids stabilized the  
94 LREEs in the Durango fluorapatite grains and prevented the formation of accessory monazite.  
95 Harlov et al. (2005) experimentally reacted natural LREE enriched Durango fluorapatite grains  
96 with 1 and 2 N HCl and H<sub>2</sub>SO<sub>4</sub> solutions at 300 – 900 °C and 0.5 – 1 GPa and reported the  
97 depletion of the REEs, Na, Si, S, and Cl in the metasomatized regions and the formation of  
98 accessory monazite, consistent with Harlov and Förster (2003). The aforementioned experiments  
99 elucidated the formation of REE-bearing monazite commonly observed in magmatic and  
100 hydrothermal systems.

101  
102 There is a dearth of published experimental data that elucidate the formation of Na-, S-, Fe- and  
103 Sr-bearing apatite in hydrothermal systems (Konecke et al., 2017; Palma et al., 2019). Existing  
104 experimental data demonstrate a relationship among Na, Si, and S in magmatic apatite that is  
105 explained by coupled substitution of Na and/or Si ions with S<sup>6+</sup> according to the following  
106 charge balanced coupled substitutions (Rouse and Dunn, 1982; Liu and Comodi, 1993; Tepper  
107 and Kuehner, 1999; Parat et al., 2011):



110 Palma et al. (2019) also reported that the concentrations of S, Fe, and Sr in fluorapatite from the  
111 magmatic-hydrothermal Mina Carmen iron oxide-apatite deposit were positively correlated with  
112 each other and that fluorapatite grains contained secondary inclusions of monazite. That the  
113 monazite is secondary is evinced by the consistent presence of hydrothermal magnetite veinlets  
114 that crosscut primary fluorapatite. Those authors did not propose an explanation for the elevated  
115 Sr concentrations in metasomatized fluorapatite from Mina Carmen, but Hughes et al. (1991) and

116 Rakovan and Hughes (2000) reported that  $\text{Sr}^{2+}$  prefers to substitute for  $\text{Ca}^{2+}$  on the M2 site in  
117 apatite while  $\text{Na}^+$  and  $\text{REE}^{3+}$  alternate occupying the M1 site. In this instance, the Na charge  
118 balances the REE via the following coupled substitution for Ca (Pan and Fleet, 2002):



120 Palma et al. (2019) reported an overall decrease of REE concentrations in the metasomatized  
121 fluorapatite grains, which suggests an influence of Sr on the coupled substitution of Na and S  
122 described in Equation 1 rather than Equation 3. Apatite in natural magmatic and magmatic-  
123 hydrothermal systems is commonly zoned with respect to F, Cl, and OH, and there is often a  
124 positive correlation among the concentrations of Cl, OH, and S contents in the metasomatized  
125 fluorapatite grains from Mina Carmen (Palma et al., 2019).

126

127 To our knowledge, there are no published experimental studies that constrain the partitioning of  
128 S and REEs between apatite and a hydrothermal fluid. Here, we report the results of a series of  
129 experiments wherein synthetic fluorapatite grains were reacted with a series of hydrothermal  
130 fluids with different compositions to assess the effects of coupled dissolution-reprecipitation and  
131 hydrothermal crystallization on the incorporation of S in metasomatized apatite. Experiments  
132 were conducted at 800 °C and 1 GPa wherein synthetic S-free fluorapatite grains were reacted  
133 with a variety of aqueous solutions containing dissolved S, Si, Fe, Ce, Sr, Na, Cl, F, and OH in  
134 varying amounts (Table 1). The new data reported here provide insight into the incorporation of  
135 S into fluorapatite that precipitates from, or re-equilibrates with, a S-bearing hydrothermal fluid.

136

137

## METHODS

138 **Experimental Methods**

139 Endmember fluorapatite (APS-102) grains used in the experiments were synthesized using the  
140 molten flux method outlined by Schettler et al. (2011) (see also Cherniak, 2000). Starting  
141 synthetic fluorapatite grains were euhedral, elongate, and homogenous in back scattered electron  
142 (BSE) image grayscale (Fig. 1). Experimental charges for metasomatism experiments consisted  
143 of 20 mg of starting synthetic fluorapatite grains (APS-102), 5 mg of H<sub>2</sub>O, 5 mg of a powdered  
144 S-bearing compound or a S-bearing solution source, and compounds possessing the necessary  
145 elements to effect charge balance for the coupled substitutions defined by Equations 1 and 2  
146 (Table 1). Experimental charges for the hydrothermal crystal growth experiments consisted of  
147 H<sub>2</sub>O, synthetic fluorapatite (APS-102) seed crystals, powdered  $\beta$ -Ca<sub>3</sub>(PO<sub>4</sub>)<sub>2</sub> (Fluka, LOT  
148 4558807/1-223043209) as a Ca and P source, and powdered NaF as a Na and F source. Here,  
149 Na<sub>2</sub>SO<sub>4</sub> served as the S source as well as providing the charge balancing cation Na<sup>+</sup> (Eqn. 1),  
150 whereas SiO<sub>2</sub> served as the source of the charge balancing cation Si<sup>4+</sup> (cf. Eqn. 2) (Table 1).  
151  
152 Charges were loaded either into 3 mm wide, 1 cm long Pt capsules for oxidized S sources or into  
153 3 mm wide, 1 cm long Au capsules for reduced S sources, and then micro arc-welded shut.  
154 Capsules were checked for leaks by first weighing, then placed in a drying oven at 110 °C for a  
155 minimum of 8 hours and then weighing again. Platinum capsules have been known to react with  
156 S to form sulfide complexes, resulting in embrittlement and/or corrosion of capsules, which can  
157 potentially result in capsule failure (Webster and Botcharnikov, 2011). In our experiments, Pt  
158 capsules containing sulfate-bearing reagents maintained capsule integrity over a 5-day duration  
159 of the experimental run.

160



161 Experiments at 800 °C and 1 GPa for 5 days were conducted for 4 Au or 4 Pt capsules at the  
162 same time using a ‘Johannes Type’ non-end load piston cylinder apparatus (Johannes et al.,  
163 1971; Johannes, 1973), a solid CaF<sub>2</sub> assembly as the pressure medium, and a cylindrical graphite  
164 oven (Angiboust and Harlov, 2017; see their Fig.3 for assembly cross section). The capsules  
165 were gently flattened and loaded vertically into an approximately 5 x 5 x 12 mm pocket in the  
166 CaF<sub>2</sub> assembly. The capsules were separated by biotite sheets to prevent them from welding  
167 together and packed with powdered CaF<sub>2</sub>. A Ni-Cr thermocouple was inserted into the CaF<sub>2</sub>  
168 assembly with the tip halfway up along the side of the experimental charges. A thermal gradient  
169 along the length of the 1 cm experiment capsule meant that either end of the capsule was  
170 approximately 20 °C lower than the temperature measured at the center. Once the CaF<sub>2</sub> assembly  
171 was loaded into the apparatus, the pressure was increased to approximately 15% below the final  
172 pressure. The temperature was increased to the final 800 °C, such that thermal expansion  
173 increased the pressure to near the desired 1 GPa. Minor adjustments were then made to achieve  
174 the final pressure, which was maintained automatically within a preset range of ± 0.015 GPa for  
175 the duration of the experiments. Experiments were quenched non-isobarically by turning off the  
176 heating current and automatic pressure control, which allowed the water cooling jackets and  
177 mass of the apparatus to cool the experiments to below 100 °C in approximately 30 seconds. The  
178 capsules were then extracted from the CaF<sub>2</sub> assembly, cleaned, and weighed to determine  
179 whether capsule integrity was maintained. Cleaned capsules that did not maintain their starting  
180 mass were discarded.

181

182 All experiment capsules were punctured, placed in a drying oven at 110 °C for 24 hrs., and  
183 weighed again to determine the amount of fluid present. The dried run products were removed

184 from the experiment capsules and rinsed three times in DI H<sub>2</sub>O to remove any solutes. A random  
185 sampling of run product grains (i.e. a literal scoop) for each experiment were then dried,  
186 mounted in epoxy, and polished for scanning electron microscopy (SEM), BSE imaging, and  
187 quantitative EPMA.

188

## 189 **Analytical Methods**

### 190 **Scanning electron microscopy (SEM) and Electron probe micro-analysis (EPMA).**

191 Carbon-coated epoxy grain mounts were first analyzed on a JEOL JSM-7800FLV SEM using an  
192 accelerating voltage of 20 kV at the Robert B. Mitchell Electron Microbeam Analysis Lab  
193 (EMAL), University of Michigan, Ann Arbor, Michigan, USA. High-contrast BSE imagery was  
194 utilized to record mineral textures of the experiment run-product fluorapatite. EPMA quantitative  
195 analyses of run-product fluorapatite compositions were conducted on a Cameca SX-100 electron  
196 microprobe (EMP) at EMAL, using a 15 keV electron beam and a beam current of 20 nA.  
197 Counting times were 10 seconds on-peak and 5 seconds off-peak for all elements measured using  
198 the mean atomic number (MAN) continuum X-ray correction method outlined in Donovan and  
199 Tingle (1996). Because of the F and Cl X-ray count rate variation in response to electron beam  
200 exposure (Goldoff et al., 2012), F and Cl were measured first as well as using Time-Dependent  
201 Intensity (TDI) corrections incorporated into ProbeForWindows software (Donovan et al., 2007).  
202 Quantitative analyses were conducted prior to the collection of representative BSE images.  
203 Multiple points on multiple grains from each experiment were selected so as to obtain a random  
204 dataset large enough for statistical consideration. Concentrations were obtained from raw counts  
205 using a ZAF intensity correction. EPMA data and standards used for peak positions are listed in  
206 the Supplementary Table 1. Wavelength dispersive spectroscopy (WDS) maps and

207 cathodoluminescence (CL) monochromatic grayscale images were collected post-quantitative  
208 analyses on the Cameca SX-100 EMP using a 15 keV electron beam, a beam current of 40 nA, a  
209 0.5  $\mu\text{m}$  step size, and a 60 ms dwell time.

210

211 **Laser ablation inductively coupled plasma mass spectrometry (LA-ICP-MS).** The  
212 concentrations of Sc, Mn, Fe, Y, Ba and REEs in the starting synthetic fluorapatite grains (APS-  
213 102) were measured by LA-ICP-MS using an ESI NWR193 laser ablation system attached to an  
214 Agilent Technologies 7900s quadrupole ICP-MS, housed at the Holder Laser Ablation ICP-MS  
215 Laboratory, University of Michigan, Ann Arbor, Michigan, USA (Supplementary Table 2).  
216 Analyses were conducted by using a 70  $\mu\text{m}$  spot size, a fluence of 1.4  $\text{J}/\text{cm}^2$ , at 6 Hz repetition,  
217 30 sec of ablation, and a 20 sec baseline. The analyte in a He carrier gas was transported from  
218 the LA system to a glass mixing bulb where the sample aerosol was mixed with Ar gas prior to  
219 the ICP-MS. Trace element concentrations and detection limits were calculated using the method  
220 outlined by Longerich et al. (1996), with the Ca concentration from EPMA analyses (Table 2) as  
221 an internal standard, and using NIST610 glass as a secondary standard. The glass standards  
222 NIST610 and NIST612 were analyzed throughout the session to correct for instrument drift.

223

224

## RESULTS

225 Major and trace element concentrations of the starting synthetic fluorapatite grains measured by  
226 EPMA are reported in Table 2. The chemical formula for run product apatite grains was  
227 calculated using 5 cations and 26 oxygens (Ketcham, 2015); with the halogen site (X) occupied  
228 by F, Cl, OH, and sulfur as  $\text{S}^{6+}$  and  $\text{S}^{4+}$  in the tetrahedral site (T). It is understood and  
229 acknowledged by the geochemical community that nano scale inclusions below a polished grain

230 surface may be present in the electron beam excitation volume. In order to address this potential  
231 issue, points selected for EPMA avoided cracks, intact and compromised fluid inclusions, and  
232 avoided regions with pervasive accessory phases (i.e. Monazite). EPMA points which yielded  
233 non-stoichiometric apatite chemical formula, insufficient sums, or indicated a secondary phase  
234 were discarded and not used in this study. Pearson correlation coefficients ( $\rho$ ) were calculated  
235 from EPMA point analyses for ion pairs of interest (Pearson, 1895). A correlation coefficient  
236 speaks to the linearity of data such that a coefficient of unity would plot on a straight line.  
237 However, a correlation coefficient does not inform on the slope of the data trend (e.g. ratios in  
238 ionic substitutions) or the extent of the data trend (e.g. minimum and maximum concentrations).  
239 We define a strong correlation as  $\rho > 0.75$ , a moderate correlation as  $0.5 < \rho < 0.75$ , and a weak  
240 correlation as  $0.25 < \rho < 0.5$ .

241

## 242 **Results from sulfate reagent experiments**

243 **Experiments at 800°C and 1 GPa involving H<sub>2</sub>O + S ± Na ± Si.** Run product  
244 fluorapatite grains from experiment FS2 (Table 1; 800 °C, 1GPa; FlAp + Na<sub>2</sub>SO<sub>4</sub> + H<sub>2</sub>O) are  
245 dominantly anhedral, occasionally fractured, present with little evidence for dissolution, and are  
246 homogenous in high-contrast BSE images (Supp. Fig. 1b). Run product fluorapatite grains from  
247 experiment FS3 (Table 1; 800 °C, 1GPa; FlAp + 1M H<sub>2</sub>SO<sub>4</sub> + SiO<sub>2</sub> + H<sub>2</sub>O) are homogenous in  
248 high-contrast BSE images, show minor evidence of dissolution with slightly rounded grains that  
249 are subhedral to anhedral and are occasionally mantled by a silicate glass that was not analyzed  
250 for its chemical composition (Supp. Fig. 1c). The compositions of run product fluorapatite grains  
251 from FS2 and FS3 are equivalent to the starting synthetic fluorapatite grains (Table 2); notably  
252 the S concentration is below the EPMA detection limit. Run product fluorapatite grains from

253 experiment FS12 (Table 1; 800 °C, 1 GPa; FlAp + Na<sub>2</sub>SO<sub>4</sub> + Na<sub>2</sub>Si<sub>2</sub>O<sub>5</sub> + H<sub>2</sub>O) are slightly  
254 rounded, subhedral to anhedral, exhibit a subtle greyscale zonation in the high-contrast BSE  
255 image, and a diffused zonation in the CL image (Fig. 2b) where darker regions are spatially  
256 correlated with increased Na, Si, and S in the WDS maps (Figs. 2c,d,e). Run product fluorapatite  
257 grains from experiment FS12 exhibit a 0.32 wt.% decrease in P to 18.22 wt.%, measurable S at  
258 347 µg/g, an increase of Na to 0.03 wt.%, and an increase of Si to 228 µg/g (Table 2). For  
259 experiment FS12 there exists a strong positive correlation between S with Na ( $\rho = +0.95$ ), and S  
260 with Si ( $\rho = +0.98$ ) for the calculated atomic proportions (Fig. 2g). The data points for Na vs. S  
261 are above and nearly straddle the stoichiometric 1:1 line whereas the Si vs. S data points with  
262 elevated S concentrations are below and subparallel to the 1:1 line (Fig. 2g). Data clusters that  
263 plot above the stoichiometric 1:1 line indicate an excess of the charge balancing cation and data  
264 clusters that plot below the 1:1 line indicate an excess of S with respect to the charge balancing  
265 cation. Run product fluorapatite grains from experiment FS15 (800 °C, 1GPa; FlAp + Na<sub>2</sub>SO<sub>4</sub> +  
266 SiO<sub>2</sub> +  $\beta$ -Ca<sub>3</sub>(PO<sub>4</sub>)<sub>2</sub> + NaF + H<sub>2</sub>O) are euhedral to anhedral, and tens to hundreds of micrometers  
267 in diameter. Aggregates of small euhedral fluorapatite grains coalesce into larger subhedral  
268 grains, where the larger grains present with subtle zonation in the high-contrast BSE and CL  
269 images (Supp. Figs. 2a,b) that is spatially correlated with elevated Na and S in the WDS maps  
270 (Supp. Figs. 2c,e). In the WDS maps of Na and S, the zonation is more apparent and exhibits a  
271 sharp reaction front separating a distinct core from the rim (Supp. Figs. 2c,e). The core appears  
272 elongate, ca. 30 µm in diameter, subhedral with distinct parallel facets, and presents topotaxial to  
273 the crystal habit of the rim. The Na and S poor core is the remnant parent crystal that has been  
274 overgrown by a new Na and S bearing daughter material that precipitates from the fluid. Run  
275 product fluorapatite grains from experiment FS15 exhibit measurable S with an average of 436

276  $\mu\text{g/g}$ , an increase of Na to ca. 0.07 wt.%, and an increase of Si to ca. 55  $\mu\text{g/g}$  (Table 2). There are  
277 two distinct populations for Na, Si, and S concentrations in the run-product fluorapatite; a S  
278 below detection limit group that plots on or near the Y-axis from measurements of grain cores  
279 and a group where S concentrations range from ca. 0.011 to 0.027 a.p.f.u. for rim measurements  
280 (Supp. Figs. 2g). There is a strong positive correlation between Na and S ( $\rho = +0.98$ ) and no  
281 correlation between Si and S ( $\rho = +0.04$ ) (Fig. 4g). The Na vs. S trend plots above and  
282 subparallel to the 1:1 atomic ratio line (Supp. Figs. 2g).

283

284 **Experiments at 800 °C and 1 GPa involving  $\text{H}_2\text{O} + \text{S} \pm \text{Na} \pm \text{Si} \pm \text{Cl} \pm \text{F} \pm \text{OH}$ .** Run  
285 product fluorapatite grains from experiment FS7 (Table 1; 800 °C, 1 GPa;  $\text{FlAp} + \text{Na}_2\text{SO}_4 +$   
286  $\text{CaCl}_2 + \text{H}_2\text{O}$ ) are subhedral to anhedral and homogenous in high-contrast BSE imagery (Supp.  
287 Fig. 1e). Run product fluorapatite grains from experiment FS16 (800 °C, 1 GPa;  $\text{FlAp} + \text{Na}_2\text{SO}_4$   
288  $+ \text{Ca}(\text{OH})_2 + \text{H}_2\text{O}$ ) are subhedral to anhedral, homogenous in high-contrast BSE imagery, with  
289 partially healed fractures and clusters of small ( $\leq 15\mu\text{m}$ ) fluorapatite grains found on rims of  
290 larger grains (Supp. Fig. 1f). Run product fluorapatite grains from experiment FS20 (Table 1;  
291 800 °C, 1 GPa;  $\text{FlAp} + \text{Na}_2\text{SO}_4 + \text{SiO}_2 + \text{CaCl}_2 + \text{H}_2\text{O}$ ) are subhedral to anhedral, with shallow  
292 etch pits, and occasional subtle rounding of corners (Supp. Fig. 1g). Large ( $> 300 \mu\text{m}$ ) elongate  
293 aggregate masses of small ( $\leq 50 \mu\text{m}$ ) euhedral to subhedral secondary quartz grains are present  
294 but were not analyzed for their chemical composition. The compositions of the run product  
295 fluorapatite grains from FS7, FS16, and FS20 are comparable to the starting synthetic  
296 fluorapatite grains (Table 2); notably, S is below the EPMA detection limit.

297

298 Run product fluorapatite grains from experiment FS8 (Table 1; 800 °C, 1 GPa; FlAp + 1M  
299 H<sub>2</sub>SO<sub>4</sub> + SiO<sub>2</sub> + CaCl<sub>2</sub> + H<sub>2</sub>O) are subhedral to anhedral with rounded margins, are homogenous  
300 in the high-contrast BSE and CL images (Supp. Figs. 3a,b) with spatially correlated elevated S  
301 and Cl in the WDS maps (Supp. Figs. 3d,f). Experiment FS8 run product fluorapatite grains  
302 exhibit a 0.25 wt.% decrease in P to 18.29 wt.%, measurable S at 105 µg/g, and an increase in Na  
303 and Si to 0.03 wt.% and 43 µg/g, respectively (Table 2). The run product halogen chemistry of  
304 experiment FS8 exhibit a 0.30 wt.% decrease of F to 3.40 wt.%, an increase of Cl to 0.44 wt.%,  
305 and an estimated OH concentration of 0.21 wt.% (Table 2). There is a weak negative statistical  
306 correlation between measured S and Si concentrations ( $\rho = -0.38$ ) and a weak positive  
307 correlation between S and Na ( $\rho = +0.36$ ). When the below detection limit data points are  
308 removed from consideration, the Na-S correlation coefficient increases to  $\rho = +0.42$  and the Si-S  
309 correlation coefficient increases to  $\rho = -0.34$ . There is a strong positive correlation between S  
310 and Cl ( $\rho = +0.91$ ) concentrations and a weak negative correlation with the estimated OH content  
311 ( $\rho = -0.31$ ). Run product fluorapatite grains from experiment FS11 (Table 1; 800 °C, 1 GPa;  
312 FlAp + Na<sub>2</sub>SO<sub>4</sub> + NaF + H<sub>2</sub>O) are subhedral to anhedral, slightly rounded with partially healed  
313 fractures, homogenous in the high-contrast BSE images (Fig. 3a), and a subtle zonation in the CL  
314 image where brighter areas are spatially correlated with elevated Na and S in the WDS maps  
315 (Figs. 3b,c,e). Run product fluorapatite grains from experiment FS11 exhibit a 0.30 wt.%  
316 decrease in the P concentration to 18.24 wt.%, measurable S at 452 µg/g, a 0.05 wt.% increase of  
317 Na to 0.07 wt.%, and a 30 µg/g increase of Si to 68 µg/g (Table 2). Experiment FS11 run product  
318 halogen chemistry exhibits a 0.07 wt.% decrease of F to 3.63 wt.% and an estimated OH  
319 concentration of 0.23 wt.% (Table 2). There is a strong positive correlation for Na and S  
320 concentrations ( $\rho = +0.98$ ) that plot above and subparallel to the 1:1 line and a weak inverse

321 correlation for Si and S ( $\rho = -0.31$ ) that plot on or near the X-axis (Fig. 3g). There is no statistical  
322 correlation for S concentrations with those of F ( $\rho = -0.22$ ), Cl ( $\rho = -0.23$ ), or OH ( $\rho = +0.22$ ).  
323 Run product fluorapatite grains from experiment FS13 (Table 1; 800 °C, 1 GPa; FlAp + Na<sub>2</sub>SO<sub>4</sub>  
324 + Na<sub>2</sub>Si<sub>2</sub>O<sub>5</sub> + CaCl<sub>2</sub> + H<sub>2</sub>O) are subhedral to anhedral, homogenous in high-contrast BSE image  
325 grayscale (Supp. Fig. 4a) with occasional aggregates of smaller ( $\leq 15\mu\text{m}$ ) grains coalescing to  
326 form larger anhedral grains. Elongate grains of accessory wollastonite (Ca<sub>3</sub>(Si<sub>3</sub>O<sub>9</sub>)) and  
327 spheroids of sodium silicate glass are present (Supp. Fig. 4a) but were not analyzed for their  
328 chemical compositions. Distinct zonation in the high-contrast CL image is visible with a spatial  
329 correlation between brighter CL areas and elevated Na, Si, and S in the WDS maps (Supp. Figs.  
330 4b,c,d,e). Run product fluorapatite grains from FS13 exhibit a 0.33 wt.% decrease of P to 18.21  
331 wt.%, measurable S at 416  $\mu\text{g/g}$ , Ca and Na average concentrations are unchanged with an  
332 increase of Si to 440  $\mu\text{g/g}$  (Table 2). Experiment FS13 run product fluorapatite grain halogen  
333 chemistry exhibits a 0.36 wt.% decrease of F to 3.34 wt.%, Cl is unchanged at 0.01 wt.%, and an  
334 estimated OH concentration of 0.46 wt.% (Table 2). There exists a strong positive correlation  
335 between S with Na ( $\rho = +0.96$ ) and Si ( $\rho = +0.99$ ) concentrations (Supp. Fig. 4g), and a  
336 moderate positive correlation with Cl ( $\rho = +0.70$ ) and estimated OH ( $\rho = +0.55$ ). The Si vs. S  
337 a.p.f.u. concentrations plot on the atomic ratio 1:1 line while the Na vs. S a.p.f.u. concentrations  
338 plot below and subparallel (Supp. Fig. 4g). Run product fluorapatite grains from experiment  
339 FS17 (Table 1; 800 °C, 1 GPa; FlAp + Na<sub>2</sub>SO<sub>4</sub> + CaCl<sub>2</sub> + Ca(OH)<sub>2</sub> + H<sub>2</sub>O) are dominantly  
340 subhedral to anhedral with partially healed fractures. Larger grains ( $> 100\mu\text{m}$ ) are occasionally  
341 an aggregate of smaller ( $\leq 15\mu\text{m}$ ) euhedral to subhedral grains (Fig. 8a). Experiment FS17 run  
342 products exhibit grain to grain variation in the high-contrast BSE image grayscale (Supp. Fig. 5a)  
343 that does not display a clear and consistent correlation with zonation in the CL image or zonation



344 in the WDS maps (Supp. Figs. 5b-f). There is a distinct zonation in the run-product WDS map of  
345 F that exhibits an inverse relationship with Cl (Supp. Figs. 5e,f) and a Na and S spatial  
346 correlation of elevated concentrations along fractures and grain margins (Supp. Figs. 5c,d). Run  
347 product fluorapatite grains from experiment FS17 exhibit a 0.32 wt.% decrease of P to 18.22  
348 wt.%, measurable S at 156  $\mu\text{g/g}$ , an increase of Na to 0.03 wt.%, and Si remains unchanged  
349 (Table 2). The Na and S concentrations plot below and appear subparallel to the 1:1 atomic ratio  
350 line while Si data points plot near the X-axis (Supp. Fig. 5g). Halogen concentrations of run  
351 products from experiment FS17 exhibit a 0.49 wt.% decrease of F to 3.21 wt.%, an increase of Cl  
352 to 0.03 wt.%, and an estimated OH concentration of 0.56 wt.% (Table 2). There is a moderate  
353 positive correlation between S and Cl ( $\rho = +0.58$ ) and between S and the estimated OH content  
354 ( $\rho = +0.55$ ).

355

356 **Experiments at 800 °C and 1 GPa involving  $\text{H}_2\text{O} + \text{S} + \text{Cl} \pm \text{Na} \pm \text{Fe} \pm \text{Sr} \pm \text{Ce}$ .** Run  
357 product fluorapatite grains from experiment FS1 (Table 1; 800 °C, 1 GPa;  $\text{FlAp} + 1\text{M H}_2\text{SO}_4 +$   
358  $\text{FeCl}_3 + \text{H}_2\text{O}$ ) are subhedral to anhedral, with few rounded grain margins (Supp. Fig. 1a). Run  
359 product fluorapatite grains from experiment FS4 (Table 1; 800 °C, 1 GPa;  $\text{FlAp} + 1\text{M H}_2\text{SO}_4 +$   
360  $\text{CeCl}_3 + \text{H}_2\text{O}$ ) are subhedral to anhedral, slightly rounded from dissolution, with sub-micrometer  
361 monazite grains found in partially healed fractures and mantling the fluorapatite grains (Supp.  
362 Fig. 1d). Run product fluorapatite grains from experiment FS21 (Table 1; 800 °C, 1 GPa;  $\text{FlAp} +$   
363  $\text{Na}_2\text{SO}_4 + \text{CeCl}_3 + \text{CaCl}_2 + \text{H}_2\text{O}$ ) are subhedral to anhedral and present with subtle rounding of  
364 corners (Supp. Fig. 1h). Sub-micrometer monazite-(Ce) grains fill fractures with little evidence  
365 of micrometer scale fluorapatite dissolution (Supp. Fig. 1h). Run product fluorapatite grains from  
366 experiments FS1, FS4, and FS21 are homogenous in the high-contrast BSE images (Supp. Fig.

367 1a,d,h). Average run product concentrations for S, Fe, and Ce from experiments FS1, FS4, and  
368 FS21 are below EPMA detection limits (Table 2).

369

370 Run product fluorapatite grains from experiment FS9 (Table 1; 800 °C, 1 GPa; FlAp + 1M  
371 H<sub>2</sub>SO<sub>4</sub> + FeCl<sub>3</sub> + CaCl<sub>2</sub> + H<sub>2</sub>O) are subhedral to anhedral and homogenous in the high-contrast  
372 BSE and CL images (Figs. 4a,b). Occasional aggregates of subhedral grains overgrown by larger  
373 anhedral masses of fluorapatite are visible in the grain mount. In contrast to the BSE and CL  
374 imagery, there exists a distinct element zonation and a strong positive spatial correlation for  
375 elevated Fe, S, and Cl in the WDS maps of the run product fluorapatite (Figs. 4d,e,f). The  
376 composition of fluorapatite grains from FS9 exhibit a decrease of P to 18.16 wt.%, measurable S  
377 at 154 µg/g, Na and Si are slightly greater at 0.03 wt.% and 48 µg/g, respectively, and  
378 measurable Fe at 0.09 wt.% (Table 2). Run product halogen concentrations in apatite grains from  
379 FS9 exhibit a decrease of F to 3.34 wt.%, an increase of Cl to 0.58 wt.%, and an estimated OH  
380 concentration of 0.20 wt.% (Table 2). The S atomic proportion exhibits a weak negative  
381 correlation with the reported trace amounts of Na ( $\rho = -0.36$ ) for all plotted data with the  
382 majority on or above the 1:1 atomic ratio line. When ion pairs with S concentrations below  
383 detection limits are removed, the Na-S correlation coefficient increases to  $\rho = +0.27$ . Data points  
384 for Si plot near and near-parallel to the X-axis (Fig. 4g), indicating no relationship with the  
385 incorporated S. The S concentrations exhibit a strong positive correlation with Fe ( $\rho = +0.75$ ) for  
386 all points measured (Fig. 4h). The reported correlation coefficient for Fe and S includes the data  
387 points that present with independent Fe and S concentrations (Fig. 4h; box outline). There is a  
388 cluster of plotted Fe concentrations that present with a linear trend that is subparallel and above  
389 the 1:1 atomic ratio line (Fig. 4h). Run product fluorapatite grains from experiment FS10 (Table

390 1; 800 °C, 1 GPa; FlAp + 1M H<sub>2</sub>SO<sub>4</sub> + CeCl<sub>3</sub> + CaCl<sub>2</sub> + H<sub>2</sub>O) are euhedral to anhedral, with a  
391 bi-modal grayscale in the high-contrast BSE and CL imagery (Figs. 5a,b). The darker, inclusion-  
392 free regions in the BSE image are marked by a sharp reaction front that is traced by micrometer  
393 to sub-micrometer scale monazite-(Ce) inclusions that separate brighter regions with numerous ≤  
394 5 μm monazite inclusions and/or grains mantling the run product fluorapatite (Fig. 5a). In the  
395 WDS maps of the run product fluorapatite grains, there exists a distinct element zonation and a  
396 positive spatial correlation for elevated Ce and S (Figs. 5c,d). The composition of the BSE darker  
397 regions in experiment FS10 exhibit a decrease in P to 18.32 wt.%, S is below EPMA detection  
398 limits, subtle increases to average Na and Si concentrations, and measurable Ce at 0.34 wt.%  
399 (Table 2). The halogen concentrations in the BSE darker regions exhibit a decrease of F to 3.43  
400 wt.%, an increase of Cl to 0.48 wt.%, and an estimated OH concentration of 0.21 wt.% (Table 2).  
401 The average concentrations of the brighter regions in fluorapatite grains from experiments FS10  
402 exhibit a further decrease in P to 18.11 wt.%, measurable S at 153 μg/g, a decrease of Ca to  
403 37.93 wt.%, and measurable Ce at 2.03 wt.% (Table 2). The Na and Si concentrations in the BSE  
404 brighter regions are comparable to the starting fluorapatite composition (Table 2). There halogen  
405 concentrations in the brighter BSE regions exhibit a further decrease of F to 3.18 wt.%, an  
406 increase of Cl to 0.83 wt.%, and an estimated OH concentration of 0.19 wt.% (Table 2). There is  
407 no statistical correlation between S and Na ( $\rho = +0.20$ ) or a positive correlation with Si ( $\rho = -$   
408 0.61) (Figs. 5d,e,f,g). There is weak statistical correlation for Ce with Na ( $\rho = +0.31$ ) and a  
409 negative correlation with Si ( $\rho = -0.51$ ) in the run-product fluorapatite concentrations. There is a  
410 strong positive spatial and chemical correlation between Ce and S ( $\rho = +0.95$ ) (Figs. 5c,d,h). Run  
411 product fluorapatite grains from experiment FS14 (Table 1; 800 °C, 1 GPa; FlAp + Na<sub>2</sub>SO<sub>4</sub> +  
412 SrCl<sub>2</sub> + H<sub>2</sub>O) are subhedral to anhedral with a bi-modal grayscale in the high-contrast BSE

413 images where the brighter regions are mantling darker cores and sometimes fluorapatite grains  
414 are mantled by masses of Cl rich SrSO<sub>4</sub> (Fig. 6a). The brighter fluorapatite regions in BSE  
415 images sometimes exhibit subtle and/or sharp zonation and can be found filling healed fractures  
416 in the darker regions. In contrast with the CL imagery, the brighter fluorapatite regions in BSE  
417 images have a strong positive spatial correlation with elevated Sr, Na, and S and a subtle positive  
418 spatial correlation with Si in the WDS maps (Figs. 6c-f). The composition of the darker  
419 fluorapatite regions in BSE images of experiment FS14 exhibit an increase of Ca to 39.26 wt.%  
420 and an estimated OH concentration of 0.21 wt.% (Table 2). The concentrations of P, Sr, Na, F,  
421 and Cl in the darker cores of the experiment run products is comparable to the concentrations in  
422 the starting fluorapatite grains and S is below the EPMA detection limit (Table 2). The  
423 composition of the brighter regions in BSE images of fluorapatite grains from experiment FS14  
424 exhibit a decrease in P to 17.17 wt.%, measurable S at 3,514 µg/g, a decrease of Ca to 32.30  
425 wt.%, an increase of Na to 0.20 wt.%, an increase of Si to 59 µg/g, and an increase of Sr to 10.24  
426 wt.% (Table 2). The halogen concentrations of the bright areas in the run product fluorapatite  
427 grains from FS14 exhibit a decrease of F to 3.29 wt.%, an increase of Cl to 0.09 wt.%, and an  
428 estimated OH concentration of 0.31 wt.% (Table 2). The darker core of the Sr-bearing  
429 fluorapatite in the BSE images (Fig. 6a) is interpreted to be the starting synthetic fluorapatite  
430 (Table 2) and the composition plots near the origin of the Na, Si, S atomic proportion plot (Fig.  
431 6g). The Sr-rich fluorapatite rims exhibit a strong positive correlation between Na and S  
432 concentrations ( $\rho = +0.99$ ) with the data plotting below and subparallel to the 1:1 atomic ratio  
433 line (Fig. 6g). The data points for the Si concentrations plot near or on the X-axis (Fig. 6g).  
434 There exists a strong positive correlation between Sr and S concentrations in the run-product  
435 fluorapatite ( $\rho = +0.99$ ).

436

### 437 **Results from sulfide reagent experiment**

438 Run product fluorapatite grains from experiment FS6-2 (Table 1; 800 °C, 1 GPa; FlAp + FeS +  
439 H<sub>2</sub>O) are anhedral, exhibit numerous, subparallel, dissolution pits 5 to 20 μm deep that extend  
440 into the grain (Fig. 7a). Two regions are visible in the high-contrast BSE images of the reacted  
441 grains, a darker homogenous core that shares a distinct reaction front with a brighter rim; the  
442 dissolution pits do not extend into the darker cores. The BSE-brighter rims exhibit a  
443 heterogenous grayscale on the micrometer scale with a combination of distinct and diffuse  
444 reaction fronts and have a strong positive spatial correlation with elevated Fe and S in the WDS  
445 maps (Figs. 7a,c,d). A minor phase consisting of 5 μm or less, bright, Fe-rich grains is present  
446 with the run product apatite grains. The Fe-rich phases are not present as inclusions in the  
447 metasomatized regions of the run product fluorapatite grains. The Fe-rich phases were not  
448 analyzed for their composition. The Fe concentration in the starting synthetic apatite is less than  
449 the LA-ICP-MS detection limit of ca. 3093 μg/kg and the S concentration is less than the EPMA  
450 detection limit of ca. 38 μg/g (Supplementary Tables 1 and 2), indicating that the observed Fe-  
451 rich phases formed from the FeS reagent added to the fluid and not from the starting synthetic  
452 apatite. The chemical composition of the BSE-darker run product fluorapatite cores from  
453 experiment FS6-2 exhibit a decrease of P to 18.40 wt.%, measurable S at 71 μg/g, an increase of  
454 Si to 57 μg/g, an estimated OH concentration of 0.21 wt.%, Ca and F concentrations comparable  
455 to the starting fluorapatite grains, and Na, Fe, and Cl concentrations below their respective  
456 EPMA detection limits (Table 2). The chemical composition of the brighter run product rims  
457 from experiment FS6-2 exhibit a decrease of P to 18.03 wt.%, measurable S at 461 μg/g, a  
458 decrease of Ca to 37.47 wt.%, measurable Fe at 2.45 wt.%, and an estimated OH concentration

459 of 0.24 wt.%. The concentrations of Na, Si, and F in the brighter rims are comparable to the  
460 starting fluorapatite grains, and Cl in the brighter regions is below the EPMA detection limit  
461 (Table 2). There is a weak-moderate correlation between Na and S concentrations in the run  
462 products ( $\rho = +0.39$ ) where the a.p.f.u. concentrations plot near the origin or near the X-axis  
463 (Fig. 7g). There is no statistical correlation between S and Si ( $\rho = -0.17$ ) nor for S with the  
464 halogens F ( $\rho = +0.18$ ), Cl ( $\rho = -0.03$ ), or OH ( $\rho = -0.18$ ). There is a strong positive correlation  
465 between Fe and S concentrations in the FS6-2 run products (Fig. 7h).

466

467

## DISCUSSION

### 468 **The role of Na and Si in hydrothermal sulfate substitution in fluorapatite**

469 Previous studies demonstrated the coupled substitutions of  $S^{6+}$  with  $Na^+$  and/or  $Si^{4+}$  (Eqns. 1 and  
470 2) for S-bearing fluorapatite crystallized from a silicate melt, whereas our experiments test the  
471 feasibility of these substitutions via a fluid-mediated process. When the Na and Si ion  
472 concentrations are compared with the S ion concentrations of run-product apatite grains from this  
473 study, there is a clear and distinct near 1:1 relationship between S and the charge balancing  
474 cation Na where the majority of data points cluster on or near the 1:1 line (Fig. 8a). The  
475 calculated statistical correlation coefficient for Na-S ion pairs for all experiments is  $\rho = +0.88$   
476 (i.e. a strong correlation). The correlation coefficient was calculated for the entire data set as we  
477 found that despite not adding a Na source to some experiments, the Na and S coupled  
478 substitution still occurred using the trace amounts of Na in the starting synthetic fluorapatite  
479 (Table 2). In contrast, when considering the Si-bearing fluid experiments there is weak evidence  
480 for a relationship between Si and S, where the majority of the EPMA data points plot near and  
481 parallel to the X-axis (Fig. 8b), indicating no substantial relationship between Si and S for the

482 experiment conditions chosen. For the aggregate Si-bearing data set a strong statistical  
483 correlation coefficient was calculated ( $\rho = +0.79$ ) and further increased to  $\rho = +0.95$  when only  
484 the experiments that indicated a Si-S coupled substitution were considered (FS12 and FS13).  
485 This overall trend is consistent with those observed in natural apatite grains from a variety of  
486 metamorphic P-T conditions as well as trends observed in experimentally crystallized apatite.  
487 The black X-symbols in Figure 8 represent average a.p.f.u. concentrations for apatite grains in  
488 metamorphic rocks from Huangmailing, Hubei and Jinping, Jiangsu, China, and apatite grains  
489 from Wilberforce, Ontario, Canada (Liu and Comodi, 1993), apatite grains from the partially  
490 metasomatized Sudbury Igneous Complex, Ontario, Canada (Warner et al., 1998), and for  
491 partially metasomatized apatite grains found in the Kiirunavaara magnetite-apatite ore bodies  
492 (Harlov et al., 2002b). These samples represent a range of metamorphic pressure and temperature  
493 conditions from 0.5 to greater than 2.8 GPa and 350 to 829 °C (Xiaochun, 1993, Liu et al., 2004;  
494 Moecher et al., 1997), which encompass the 1GPa and 800 °C experimental conditions of this  
495 study. We find that our data exhibit overlap with the black symbols representing apatite  
496 compositions from metamorphic terranes, where they cluster along and near the 1:1 line in the  
497 Na-S atomic plot (Fig. 8a) and trace amounts plot on or near the 1:1 line in on the Si-S atomic  
498 plot (Fig. 8b). The grey polygons in Figure 8 represent the approximate regions of plotted Na vs.  
499 S and Si vs. S a.p.f.u. concentrations of run-product apatite grains (Parat et al., 2011) from the S  
500 partitioning apatite-melt experiments of Parat and Holtz (2004, 2005) and Parat et al. (2008) that  
501 exhibit much less overlap with our experimental results when compared to the metamorphic  
502 apatite (Figs. 8a,b).

503

504 From the overall Na vs. S trend that is near-parallel to and straddles the 1:1 atomic proportion  
505 line (Fig. 8a) and the reported Pearson correlation coefficients, it is clear that, for the fluid  
506 compositions and P-T conditions chosen, a stronger relationship exists between S and the charge  
507 balancing cation Na (Eqn. 1). Whereas for the Si and S atomic plot, the natural metamorphic  
508 apatite plot near the origin or near and parallel to the Y-axis while the experiment run-product  
509 apatite compositions plot near the origin or near and parallel to the X-axis, indicating the  
510 independent incorporation of Si and/or S i.e. not through the Si-S coupled substitution (Eq. 2),  
511 and few data points plot near the 1:1 line and up to ca. 0.035 a.p.f.u. (Fig. 8b), indicating that the  
512 coupled substitution between Si and S is secondary (Eqn. 2).

513  
514 We acknowledge that of our experiments testing the Si-S coupled substitution, few resulted in  
515 appreciable concentrations of Si and S. We suspect that this is from the Si reagents chosen:  
516 powdered  $\text{Na}_2\text{Si}_2\text{O}_5$  and powdered crystalline  $\text{SiO}_2$ . Experiments FS12 and FS13 used  $\text{Na}_2\text{Si}_2\text{O}_5$   
517 and are the only two experiments that yielded appreciable Si-S concentrations (Table 2) and  
518 exhibit Si-S trends that are comparable to the natural metamorphic apatite (Fig. 8b, cf. Fig.2 and  
519 Supplementary Fig. 4).  $\text{Na}_2\text{Si}_2\text{O}_5$  (Industrial reagent nomenclature: SKS-6) is a commercial grade  
520 water softening agent that is readily soluble in  $\text{H}_2\text{O}$  at room temperature, saturates a fluid of  
521 amorphous silica and aqueous Na (Coker and Rees, 1993), and is a synthetic analog of the  
522 naturally occurring natrosilite. Thermodynamic models demonstrate that amorphous silica (e.g.  
523 SKS-6) is more soluble than crystalline  $\text{SiO}_2$  in pure  $\text{H}_2\text{O}$ , but the overlap in the P-T limitations  
524 of the models do not include our experiment P-T conditions (Fournier and Rowe, 1977; Fournier  
525 and Potter II, 1982; Manning, 1994; Dolejš and Manning, 2010; Karásek et al. 2013). However,



526 this does not change our conclusion of a Na-S coupled substitution being preferred to a Si-S  
527 coupled substitution.

528

529 It is not uncommon for Na a.p.f.u. concentrations to plot above the stoichiometric 1:1 line  
530 indicating an excess of Na with respect to the coupled, charge balanced element being  
531 substituted in the apatite crystal structure, such as S or REEs (Fig. 8a). This can be corrected for  
532 natural concentrations by subtracting the ionic influences of elements that compete with the  
533 element of interest, e.g. ionic Si-(Ce+Na) vs. ionic S (Peng et al., 1997). However, correcting for  
534 the trace amounts of the REEs and Y in the starting synthetic fluorapatite (Supplementary Table  
535 2) does not completely account for the excess Na with respect to S. Therefore, we suggest the  
536 known substitution of Na for Ca and a vacancy on the halogen site that allows for an overall  
537 neutral charge balance ( $\text{Na}^+ + \text{Vac.} = \text{Ca}^{2+} + \text{X}^-$ ; Pan and Fleet, 2002):

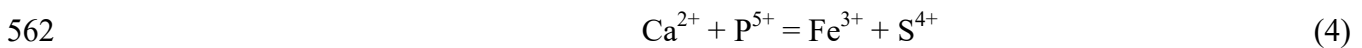
538

539 The results of our experiments demonstrate the successful Na and Si charge balanced sulfate  
540 coupled substitutions (Eqns. 1 and 2) during hydrothermal alteration and precipitation of the  
541 mineral apatite, affirming the mineral apatite as a recorder of S, Na, and Si in a hydrothermal  
542 fluid. When comparing the initial S concentration in the starting fluids (Table 1) to the measured  
543 average S concentration in the respective run-products (Table 2), it is clear that the activity  
544 of Na and Si in the fluid is the limiting factor. However, experimentation that further constrains  
545 the concentrations of Na, Si, and S in the starting and run-product fluid and apatite grains is  
546 required to quantify the partitioning of S, Na, and Si between metasomatized apatite and a  
547 hydrothermal fluid as a function of their respective concentrations.

548

549 **Fluorapatite as a recorder of metal content in hydrothermal fluids**

550 Apatite supergroup minerals can substitute a variety of metals for Ca in the crystal structure (e.g.  
551  $\text{Pb}^{2+}$ ,  $\text{Ba}^{2+}$ ,  $\text{Sr}^{2+}$ ,  $\text{Mn}^{2+}$ ,  $\text{Na}^+$ ,  $\text{Ce}^{3+}$ ,  $\text{La}^{3+}$ ,  $\text{Y}^{3+}$  and  $\text{Bi}^{3+}$ ; Pasero et al., 2010). Experiment FS1  
552 reacted the starting synthetic fluorapatite with an Fe-bearing fluid with no Na or Si added as a  
553 reagent, which yielded run-products with little textural or chemical evidence that the starting  
554 fluorapatite had reacted with the fluid (Supp. Fig. 1a; Table 2). Experiment FS9 further increased  
555 the Cl activity in the fluid with the addition of  $\text{CaCl}_2$ , which resulted in partially metasomatized  
556 fluorapatite with measurable concentrations of Fe and S in the altered areas (Table 2). For the  
557 calculated a.p.f.u. concentrations, there is no statistical correlation indicates a coupled  
558 substitution between S and the trace amounts of the charge balancing cations Na and Si that  
559 might be sourced from the dissolution of the synthetic apatite. However, there is a strong positive  
560 correlation between Fe and S (Fig. 4h), which we suggest implies a previously unexplored  
561 coupled substitution between ferric iron and sulfite:

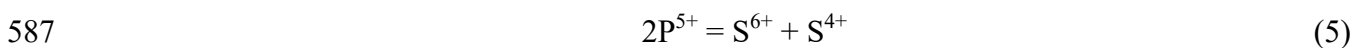


563  
564 At the intrinsic  $f\text{O}_2$  buffering of the ‘Johannes type’ piston cylinder apparatus is assumed to be  
565 between the graphite-carbon-carbon monoxide (CCO) buffer (imposed by piston cylinder  
566 graphite oven) and approximately the nickel – nickel oxide (NNO) buffer (Matjuschkin et al.,  
567 2015), ferrous and ferric iron exist. Due to the likely coexistence of  $\text{Fe}^{2+}$  and  $\text{Fe}^{3+}$  in the fluid, the  
568 observed correlation between Fe and S (Fig. 4h), and the lack of a significant correlation  
569 between S and the other known charge balancing cations (Fig. 4g), we propose Equation 4 to  
570 explain sulfite incorporation in apatite. This is supported by evidence that synthetic apatite  
571 grown from a fluid can be doped with  $\text{Fe}^{3+}$  (Low et al., 2008; Salviulo et al., 2010). We stress

572 that we were unable to determine the oxidation states of Fe in our run-product fluorapatite as this  
573 requires the use of micro X-ray absorption near edge structure ( $\mu$ -XANES) spectroscopy at the  
574 Fe *K*-edge. However, these results highlight the ability of apatite to record fluid compositions  
575 and potentially multiple species of redox sensitive metals. Further redox and crystal structure  
576 analyses, which is beyond the scope of this study, will be required to better understand the site  
577 occupancy (M1 vs. M2) and the effects of the smaller Fe<sup>2+</sup> and Fe<sup>3+</sup> cations (Shannon, 1976) on  
578 the fluorapatite crystal structure.

579

580 If the 0.09 wt.% Fe incorporated into the run-product apatite for experiment FS9 is not some  
581 ratio of Fe<sup>2+</sup>/Fe<sup>3+</sup>, then all must have been incorporated as a direct substitution of Fe<sup>2+</sup> for Ca<sup>2+</sup>,  
582 leaving one method for the incorporation of the measured S. Sulfur in magmatic-hydrothermal  
583 fluids can be present as S<sup>2-</sup>, S<sup>4+</sup>, and S<sup>6+</sup> where the proportion of each is controlled by *f*O<sub>2</sub>  
584 (Binder and Keppler, 2011; Binder et al., 2018). Konecke et al. (2017) reported the presence of  
585 S<sup>4+</sup> in the metasomatized regions of Mina Carmen fluorapatite and proposed the following  
586 polyvalent S coupled substitution (Konecke et al., 2017a; Kim et al., 2017):



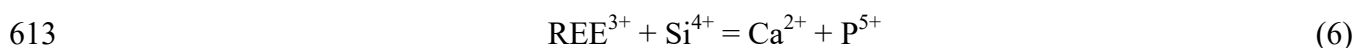
588

589 We suggest that this coupled sulfate-sulfite substitution explains the perceived excess S in all of  
590 our run-products with respect to Equations 1 and 2 (i.e. more S than Na or Si allows). Without a  
591 coupled substitution with Fe<sup>3+</sup>, then the 154  $\mu\text{g/g}$  of measured S (Table 2) would be from the  
592 sulfite-sulfate coupled substitution (Eq.5).

593

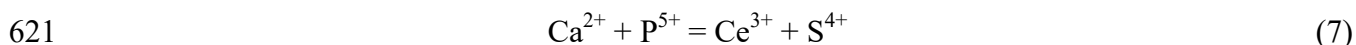
594 Strontium is a minor element commonly found in fluorapatite (Nash, 1984) and exhibits a unique  
595 relationship with Na and the REEs in fluorapatite. When Sr is substituted into the apatite crystal  
596 structure, it exhibits a preferential occupancy of the M2 site, which is normally occupied by the  
597 smaller  $\text{Ca}^{2+}$ , while the also larger Na and the REEs (Shannon, 1976) alternate occupying the M1  
598 site (Hughes et al., 1991; Rakovan and Hughes, 2000). Due to the positive spatial and statistical  
599 correlations between Na and S enrichment, spatial correlations between Sr and S enrichment in  
600 the run-product Sr-bearing fluorapatite (Figs. 6c,d,e,g), and the known site occupancies of Sr and  
601 Na in strontian apatite we suggest that the presence of Sr in a hydrothermal fluid has significant  
602 potential to promote Equation 1 over Equation 3, when the concentration of REEs in the  
603 hydrothermal fluid are vanishingly low (i.e. REEs were not added to the experiment fluid and  
604 vanishingly low concentrations as a potential source are present in the starting apatite; cf.  
605 Supplementary Table 2), but is not a component in the charge balanced coupled substitution  
606 formula of S. Experiment FS14 yielded texturally and compositionally zoned Sr-bearing  
607 fluorapatite grains that yielded the greatest average S concentration for all experiments in this  
608 study (3,514  $\mu\text{g/g}$ ; Table 2).

609  
610 It is well known that the mineral apatite is one of the principal hosts of REEs in geologic systems  
611 (Nash, 1984) and that they commonly substitute into the crystal structure via coupled substitution  
612 with Na (Eqn. 1) and Si (Pan and Fleet, 2002):



614 Experiment FS10, which reacted the starting synthetic fluorapatite with a S-, Ce-, and Cl-bearing  
615 fluid, yielded a texturally and compositionally zoned run product fluorapatite (Fig. 5a; Table 2).  
616 No observable spatial distribution or measured atomic proportions were observed that would

617 indicate a S coupled substitution with the trace amounts of Na and Si present in the starting  
618 synthetic fluorapatite, nor for Ce with Na or Si (Figs. 5e,f,g). However, there is a strong positive  
619 spatial and statistical chemical correlation between Ce and S (Figs. 5c,d,h). From these  
620 observations, we propose the following coupled substitution between  $\text{Ce}^{3+}$  and  $\text{S}^{4+}$ :



622  
623 It is known that REE-bearing phosphates form at the expense of the host apatite grain via  
624 coupled dissolution-reprecipitation of the host apatite by a hydrothermal fluid and that a coeval  
625 decrease in Na, Si, and S can occur (Harlov et al., 2002a, 2005; cf. Our Eqns. 1,2,3, and 6).  
626 During growth of secondary monazite-(Ce) from Ce- and S-bearing apatite grains, sulfate will  
627 commonly substitute for phosphate in the monazite crystal structure (Laurent et al., 2016).  
628 However, the dependence of both the REEs and S on Na and Si for coupled substitutions into the  
629 apatite crystal structure, the need for ionic corrections to natural apatite REE and S a.p.f.u. plots  
630 (Peng et al., 1997; Streck and Dilles, 1998), the known REE-sulfate complexes in a hydrothermal  
631 fluid for transport and deposition (Banks et al., 1994; Migdisov et al., 2016), and the  
632 aforementioned substitution of S during the growth of REE-phosphates, all indicate an intrinsic  
633 and non-trivial relationship between S, the REEs, and the apatite supergroup.

634  
635 The results of these metal-focused hydrothermal fluid alteration experiments demonstrate that  
636 apatite records information about the metal budget of hydrothermal fluids. The results reported  
637 here document previously unrecognized interdependencies between the substitution of S and the  
638 metals Fe, Sr, and Ce into the apatite crystal structure. The mineral apatite records their presence  
639 using the direct substitution of divalent cations, the coupled substitution of non-divalent cations

640 (e.g.  $\text{Ce}^{3+}$ ) with  $\text{Na}^+$  and/or  $\text{Si}^{4+}$ , and our proposed coupled substitutions with S. These  
641 experiments underscore the necessity for further investigation into the redox state of Fe in the  
642 run-product apatite grains and structural refinements of the run-product crystal structure to better  
643 understand the site specific effects of these metal and S substitutions on the apatite crystal  
644 structure.

645

#### 646 **Effects of metasomatized fluorapatite halogen chemistry on fluid-mediated S substitutions**

647 Fluorapatite is the most common apatite end-member in magmatic systems (Piccoli and Candela,  
648 2002; references therein) and changes to the apatite halogen chemistry reflects the composition  
649 of the silicate melt during primary apatite crystallization (Webster and Piccoli, 2015; references  
650 therein) and magmatic-hydrothermal fluids during metasomatic alteration (Harlov, 2015; Spear  
651 and Pyle, 2002; Zhu and Sverjensky, 1991). Literature describing the apatite supergroup often  
652 define members by their halogen chemistry (e.g. Sulphato-silicates  $[\text{Ca}_{10}(\text{SiO}_4)_3(\text{SO}_4)_3(\text{X})_2]$  -  
653 ellestadite-(OH) and ellestadite-(F)) (Pasero et al., 2010), which leads to our hypothesis that  
654 apatite halogen chemistry effects the substitution of S in fluorapatite.

655

656 Experiment FS11 is a control group experiment whereby saturating the fluid with a F source  
657 (NaF) the run products remained a F-dominant apatite (Harlov, 2015; Spear & Pyle, 2002; Zhu  
658 and Sverjensky, 1991). Experiment FS8 reacted the synthetic fluorapatite with a Na-free fluid  
659 saturated with Si and Cl to explore the effects of Cl substitution on Equation 2. The run product  
660 fluorapatite grains from experiment FS8 exhibit a minor incorporation of Cl and estimated OH  
661 (Table 2). There is a weak negative correlation between S and Si, contrary to what was  
662 anticipated. Instead, there is a weak correlation between S and Na which we suggest indicates

663 that the trace amounts of Na in the starting fluorapatite charge balanced the incorporation of S in  
664 the run-products (Table 2). Experiment FS17 utilized  $\text{Ca}(\text{OH})_2$  to increase the activity of OH in  
665 the fluid and promote the incorporation of OH into the apatite crystal structure to explore the  
666 effects of OH on Equation 1. EPMA analyses indicate that we were able to successfully  
667 incorporate OH into the run product apatite with a reduction of F, a minor Cl incorporation, and  
668 an increase of the estimated OH content (Table 2). Experiment FS13 reacted synthetic  
669 fluorapatite with a Na-, Si-, and Cl-bearing fluid in order to explore the effects of Cl substitution  
670 on Equations 1 and 2. EPMA analyses reveal a decrease in F, no appreciable change to Cl, and  
671 an increase of the estimated OH concentration (Table 2).

672  
673 Of the experiments conducted testing the effects of the halogens F, Cl, and OH in the fluid on  
674 Equations 1 and 2, FS11 retained halogen concentrations similar to the starting apatite grains and  
675 yielded the greatest average measured S concentration (Fig. 9; Table 2). We suggest that in this  
676 instance the reincorporation of Ca was suppressed during dissolution-reprecipitation by the  
677 formation of  $\text{CaF}_2$  using the excess F in the fluid (Harlov et al., 2006), thereby promoting the  
678 substitution of Na and S in run products from experiment FS11 (Fig. 3g). Experiment FS13  
679 exhibits the next greatest S concentration with a moderate estimated OH concentration and a  
680 minor Cl concentration (Fig. 9; Table 2) Experiments FS17 and FS8 exhibit the lowest S  
681 concentrations of the 4 experiments despite the greatest estimated OH and Cl concentrations,  
682 respectively (Fig. 9; Table 2). We suggest that the moderate to strong correlations between S and  
683 Cl concentrations, and the moderate correlation with estimated OH concentrations in the run  
684 products demonstrate an effect of apatite halogen chemistry on the incorporation of S in apatite.  
685 The halogen Cl has a larger ionic radius when compared to F and OH, is disordered above or

686 below the mirror planes in the unit cell which affects adjacent site occupancies, and has  
687 cascading effects on interatomic bond lengths and forces (Hughes et al., 1989). The complex and  
688 intricate effects of halogen site chemistry on the apatite crystal structure and the relatively  
689 inconclusive results of our halogen alteration experiments stress the importance of conducting  
690 detailed structural refinement studies to better understand the control of halogen site chemistry  
691 on the substitution of minor and trace elements on the M- and T-sites in the apatite crystal  
692 structure.

693  
694 A positive relationship is observed between the initial S and Cl concentrations in the fluid (Table  
695 1) and the S and Cl concentrations in the run-product apatite grains (Table 2) from experiments  
696 FS11, FS13, FS17, and FS8. For these four experiments, FS11 had the greatest initial S content  
697 in the fluid and yielded the greatest S concentration in the run-products while FS8 had the  
698 greatest initial Cl content in the fluid and yielded the greatest Cl content in the run-products. This  
699 trend for the F, Cl, and estimated OH concentrations in the experiment run-products agrees with  
700 the dependence of apatite halogen site chemistry on the activity of F, Cl, and OH in a  
701 hydrothermal fluid (Harlov, 2015; Spear and Pyle, 2002; Zhu and Sverjensky, 1991). However,  
702 this trend is not true for S. Experiment FS14 run-products yielded the greatest average S content  
703 of all experiments with ca. 7.6 wt.% S in the starting fluid composition while experiment FS6-2  
704 yielded significantly less S in the run-products despite an initial fluid composition of ca. 22.3  
705 wt.% S. These observations reinforce the hypothesis that the concentrations of charge balancing  
706 elements is the limiting factor for S substitutions.

707



708 In the WDS maps of some experiments, the zonation of F or Cl is diffuse and in contrast to the  
709 sharp reaction fronts visible for other elements (e.g. Figs. 2e,f). Sharp reaction fronts in  
710 metasomatized fluorapatite are indicators of dissolution-reprecipitation and diffuse reaction  
711 fronts are attributed to volume diffusion (Harlov et al. 2005; Putnis, 2002, 2009; Altree-Williams  
712 et al., 2015), illustrating two distinct methods of re-equilibration. However, from the work of  
713 others we know that electron beam induced diffusion of F and Cl in fluorapatite is common  
714 (Stormer et al., 1993) and that the beam current affects the rate of diffusion (Goldoff et al.,  
715 2012). This indicates that the alteration to the fluorapatite chemistry is a result of dissolution-  
716 reprecipitation and that the diffuse reaction fronts visible in the F WDS map are a result of the  
717 beam current and dwell time used for EPMA WDS data collection.

718

### 719 **Hydrothermal sulfide substitution in fluorapatite**

720 Experiment FS6-2, which reacted the starting synthetic apatite grains with an FeS-bearing  
721 aqueous fluid to assess whether reduced S will substitute for F, Cl, and OH in apatite grains  
722 reacted with a hydrothermal fluid. If the reduced S substituted for F in fluorapatite run-products,  
723 we would expect to see an inverse relationship between S and F concentrations. However, no  
724 statistically significant inverse correlation was observed for a.p.f.u. concentrations between S  
725 and F, nor Cl or OH concentrations. Despite the textural differences, the results of experiment  
726 FS6-2 (Figs. 7c,d) are similar to those of FS9 (Figs. 4d,e) where there is a clear positive spatial  
727 correlation between Fe and S, and an unexpected strong positive correlation between the  
728 calculated ionic concentrations of Fe and S in the run-product fluorapatite for experiment FS6-2  
729 (Fig. 7h).

730

731 Given the possible range of intrinsic  $fO_2$  buffering of the piston cylinder experiment apparatus  
732 (CCO to NNO), it is reasonable to assume the coexistence of  $S^{2-}$ ,  $S^{4+}$ , and  $S^{6+}$  in the fluid (Binder  
733 and Keppler, 2011; Binder et al., 2018). However, without a clearly constrained intrinsic  
734 buffering of the piston cylinder apparatus, it is impossible to infer an approximate ratio of  $S^{6+}/\Sigma S$   
735 for the hydrothermal fluid. Therefore, we cannot confirm whether  $S^{2-}$  or  $S^-$  were present in great  
736 enough abundance to react with the synthetic fluorapatite. Due the strong positive correlation  
737 between Fe and S, and the lack of an inverse correlation between S and F, we suggest that the  
738 results of experiment FS6-2 provide additional evidence for a potential  $Fe^{3+}$  and  $S^{4+}$  coupled  
739 substitution (Eqn. 4).

740

741

## IMPLICATIONS

742 The data reported here document that fluorapatite, which experiences hydrothermal  
743 metasomatism, preserves the chemical signature of the metasomatic fluid. Palma et al. (2019)  
744 conducted textural, micro-analytical, and isotopic analyses on metasomatized primary  
745 fluorapatite grains from the Mina Carmen IOA deposit in the Chilean iron belt. They propose  
746 that an oxidized Cl-OH-S bearing magmatic-hydrothermal fluid reacted with the primary  
747 magmatic fluorapatite and resulted in the partially metasomatized Cl-OH apatite rims that are  
748 enriched in Na, S, Fe, and Sr. The results of our experiments are consistent with their hypothesis  
749 that metasomatized fluorapatite will incorporate the volatiles Cl, OH, and S during the  
750 dissolution-reprecipitation process and that the dominant S substitution in apatite occurs by  
751 coupled substitution with Na (Eqn. 1; Fig.8a) and not with Si (Eqn. 2; Fig.8b). We suggest that  
752 Sr in the magmatic-hydrothermal fluid likely promoted the Na-S coupled substitution as  
753 evidenced by the coeval enrichment of Sr in the metasomatized regions of the Mina Carmen

754 apatite grains. We caution that the Na and S concentrations in the metasomatized regions of  
755 Mina Carmen apatite should not be used to approximate Na or S concentrations in the fluid until  
756 the influence of Sr on Equation 1 is better understood. The demonstrated fluid mediated Fe  
757 incorporation in our experiment run-products suggest that the metasomatizing fluid was likely  
758 enriched in Fe, supported by the reported cross-cutting relationship between magnetite veinlets  
759 and the Fe-enriched Mina Carmen fluorapatite.

760

761 Boyce et al. (2014) proposed a fractional crystallization model to explain an observed core to rim  
762 S enrichment and F-Cl-OH transition in apatite grains from lunar mare basalts. This model was  
763 refuted by Konecke et al. (2017b) when they experimentally demonstrated that the proposed  
764 lunar melt composition could not account for the S concentrations in the apatite grains. They  
765 instead proposed a cryptic metasomatic event where the primary Cl-OH-S-poor lunar apatite  
766 grains were altered by a S-Cl-bearing fluid that resulted in the enriched rims. The results of our  
767 experiments demonstrate the metasomatic enrichment of Cl, OH, and S in a relatively S- and Cl-  
768 free primary fluorapatite and support the cryptic metasomatism hypothesis of Konecke et al.  
769 (2017b). Boyce et al. (2014) also reported the apparent coeval enrichment of Fe, Si, and Ce with  
770 the volatiles Cl and OH. This core to rim enrichment is similar to that reported by Palma et al.  
771 (2019) for the metasomatized Mina Carmen fluorapatite grains and our experiments demonstrate  
772 the fluid-mediated enrichment of these elements in metasomatized run-product fluorapatite  
773 grains.

774

775

### **Acknowledgements**

776 This research was funded by the U.S. National Science Foundation (NSF) grants 1924142 and  
777 2214119 and an NSF Graduate Research Fellowship to J.C. We thank Monika Koch-Müller for  
778 graciously hosting J.C. at the GFZ, Potsdam, DE. We thank Owen K. Neill for his assistance  
779 with microprobe analysis at the Robert B. Mitchell Electron Microbeam Analysis Lab,  
780 University of Michigan, Ann Arbor, Michigan, USA, and Robert Holder for his assistance with  
781 laser ablation inductively coupled plasma mass spectrometry analysis at the Holder Laser  
782 Ablation ICP-MS Laboratory, University of Michigan, Ann Arbor, Michigan, USA.  
783

- 785 Akella, J., Vaidya, S.N., and Kennedy, G.C. (1969) Melting of Sodium Chloride at Pressures to  
786 65 kbar. *Physical Review*, 185(3), 1135-1140.  
787
- 788 Atree-Williams, A., Pring, A., Ngothai, Y., and Brugger, J. (2015) Textural and compositional  
789 complexities resulting from coupled dissolution–reprecipitation reactions in geomaterials.  
790 *Earth-Science Reviews*, 150, 628-651.  
791
- 792 Andersson, S.S., Wagner, T., Jonsson, E., Fusswinkel, T., and Whitehouse, M.J. (2019) Apatite  
793 as a tracer of the source, chemistry and evolution of ore-forming fluids: The case of the  
794 Olserum-Djupedal REE-phosphate mineralisation, SE Sweden. *Geochimica et*  
795 *Cosmochimica Acta*, 255, 163-187.  
796
- 797 Angiboust, S., and Harlov, D. (2017) Ilmenite breakdown and rutile-titanite stability in  
798 metagranitoids: Natural observations and experimental results. *American Mineralogist*,  
799 102(8), 1696-1708.  
800
- 801 Banks, D.A., Yardley, B.W.D., Campbell, A.R., and Jarvis, K.E. (1994) REE composition of an  
802 aqueous magmatic fluid: A fluid inclusion study from the Capitan Pluton, New Mexico,  
803 U.S.A. *Chemical Geology*, 113(3-4), 259-272.  
804
- 805 Belousova, E., Griffin, W., O'Reilly, S.Y., and Fisher, N. (2002) Apatite as an indicator mineral  
806 for mineral exploration: trace-element compositions and their relationship to host rock  
807 type. *Journal of Geochemical Exploration*, 76(1), 45-69.  
808
- 809 Binder, B., and Keppler, H. (2011) The oxidation state of sulfur in magmatic fluids. *Earth and*  
810 *Planetary Science Letters*, 301(1-2), 190-198.  
811
- 812 Binder, B., Wenzel, T., and Keppler, H. (2018) The partitioning of sulfur between  
813 multicomponent aqueous fluids and felsic melts. *Contributions to Mineralogy and*  
814 *Petrology*, 173(2), 18.  
815
- 816 Boyce, J.W., Tomlinson, S.M., McCubbin, F.M., Greenwood, J.P., and Treiman, A.H. (2014)  
817 The lunar apatite paradox. *Science*, 344(6182), 400-2.  
818
- 819 Cherniak, D.J. (2000) Rare earth element diffusion in apatite. *Geochimica et Cosmochimica*  
820 *Acta*, 64(22), 3871-3885.  
821
- 822 Chew, D.M., and Spikings, R.A. (2015) Geochronology and Thermochronology Using Apatite:  
823 Time and Temperature, Lower Crust to Surface. *Elements*, 11(3), 189-194.  
824
- 825 Coker, E.N., and Rees, L.V.C. (1993) Solubility and water-softening properties of a crystalline  
826 layered sodium silicate, SKS-6. *Journal of Materials Chemistry*, 3(5).  
827

- 828 Dolejš, D., and Manning, C. (2010) Thermodynamic model for mineral solubility in aqueous  
829 fluids: theory, calibration and application to model fluid-flow systems. *Geofluids*, 10(1-  
830 2), 20-40.  
831
- 832 Donovan, J.J., and Tingle, T.N. (1996) An improved mean atomic number background  
833 correction for quantitative microanalysis. *Microscopy and Microanalysis*, 2(1), 1-7.  
834
- 835 Donovan, J., Kremser, D., Fournelle, J., and Goemann, K. (2007) Probe for Windows user's  
836 guide and reference, enterprise edition. Probe Software, Inc., Eugene, OR.  
837
- 838 Enkhbayar, D., Seo, J., Choi, S.-G., Lee, Y.J., and Batmunkh, E. (2016) Mineral Chemistry of  
839 REE-Rich Apatite and Sulfur-Rich Monazite from the Mushgai Khudag, Alkaline  
840 Volcanic-Plutonic Complex, South Mongolia. *International Journal of Geosciences*,  
841 07(01), 20-31.  
842
- 843 Goldoff, B., Webster, J.D., and Harlov, D.E. (2012) Characterization of fluor-chlorapatites by  
844 electron probe microanalysis with a focus on time-dependent intensity variation of  
845 halogens. *American Mineralogist*, 97(7), 1103-1115.  
846
- 847 Harlov, D.E. (2015) Apatite: A Fingerprint for Metasomatic Processes. *Elements*, 11(3), 171-  
848 176.  
849
- 850 Harlov, D.E., and Förster, H.J. (2003) Fluid-induced nucleation of (Y+REE)-phosphate minerals  
851 within apatite: Nature and experiment. Part II. Fluorapatite. *American Mineralogist*, 88(8-  
852 9), 1209-1229.  
853
- 854 Harlov, D.E., Förster, H.-J., and Nijland, T.G. (2002a) Fluid-induced nucleation of (Y + REE)-  
855 phosphate minerals within apatite: Nature and experiment. Part I. Chlorapatite. *American*  
856 *Mineralogist*, 87(2-3), 245-261.  
857
- 858 Harlov, D., Renzulli, A., and Ridolfi, F. (2006) Iron-bearing chlor-fluorapatites in crustal  
859 xenoliths from the Stromboli volcano (Aeolian Islands, Southern Italy): an indicator of  
860 fluid processes during contact metamorphism. *European Journal of Mineralogy*, 18(2),  
861 233-241.  
862
- 863 Harlov, D.E., Wirth, R., and Förster, H.-J. (2005) An experimental study of dissolution-  
864 reprecipitation in fluorapatite: fluid infiltration and the formation of monazite.  
865 *Contributions to Mineralogy and Petrology*, 150(3), 268-286.  
866
- 867 Harlov, D.E., Andersson, U.B., Förster, H.-J., Nyström, J.O., Dulski, P., and Broman, C. (2002b)  
868 Apatite-monazite relations in the Kiirunavaara magnetite-apatite ore, northern Sweden.  
869 *Chemical Geology*, 191(1-3), 47-72.  
870
- 871 Hughes, J.M., and Rakovan, J.F. (2015) Structurally Robust, Chemically Diverse: Apatite and  
872 Apatite Supergroup Minerals. *Elements*, 11(3), 165-170.  
873

874 Hughes, J.M., Cameron, M., and Crowley, K.D. (1989) Structural variations in natural F, OH,  
875 and Cl apatites. *American Mineralogist*, 74(7-8), 870-876.  
876

877 Hughes, J.M., Cameron, M., and Crowley, K.D. (1991) Ordering of divalent cations in the  
878 apatite structure: Crystal structure refinements of natural Mn- and Sr-bearing apatite.  
879 *American Mineralogist*, 76(11-12), 1857-1862.  
880

881 Johannes, W. (1973) A simplified piston-cylinder apparatus of high precision. *Neues Jahrbuch*  
882 *für Mineralogisch Monatlich*, 7(8), 331-351.  
883

884 Johannes, W., Bell, P.M., Mao, H.K., Boettcher, A.L., Chipman, D.W., Hays, J.F., Newton,  
885 R.C., Seifert, F. (1971) An interlaboratory comparison of piston-cylinder pressure  
886 calibration using the albite-breakdown reaction. *Contributions to Mineralogy and*  
887 *Petrology*, 32, 24-38.  
888

889 Karásek, P., Šťavíková, L., Planeta, J., Hohnová, B., and Roth, M. (2013) Solubility of fused  
890 silica in sub-and supercritical water: Estimation from a thermodynamic model. *The*  
891 *Journal of Supercritical Fluids*, 83, 72-77.  
892

893 Ketcham, R.A. (2015) Technical Note: Calculation of stoichiometry from EMP data for apatite  
894 and other phases with mixing on monovalent anion sites. *American Mineralogist*, 100(7),  
895 1620-1623.  
896

897 Kim, Y.J., and Konecke, B. (2022) An ab-initio study on the thermodynamics of disulfide,  
898 sulfide, and bisulfide incorporation into apatite and the development of a more  
899 comprehensive temperature, pressure, pH, and composition-dependent model for ionic  
900 substitution in minerals. *The American mineralogist*.  
901

902 Kim, Y., Konecke, B., Fiege, A., Simon, A., and Becker, U. (2017) An ab-initio study of the  
903 energetics and geometry of sulfide, sulfite, and sulfate incorporation into apatite: The  
904 thermodynamic basis for using this system as an oxybarometer. *American Mineralogist*,  
905 102(8), 1646-1656.  
906

907 Konecke, B.A., Fiege, A., Simon, A.C., Parat, F., and Stechern, A. (2017a) Co-variability of  
908 S<sup>6+</sup>, S<sup>4+</sup>, and S<sup>2-</sup> in apatite as a function of oxidation state: Implications for a new  
909 oxybarometer. *American Mineralogist*, 102(3), 548-557.  
910

911 Konecke, B.A., Fiege, A., Simon, A.C., and Holtz, F. (2017b) Cryptic metasomatism during late-  
912 stage lunar magmatism implicated by sulfur in apatite. *Geology*.  
913

914 Konecke, B.A., Fiege, A., Simon, A.C., Linsler, S., and Holtz, F. (2019) An experimental  
915 calibration of a sulfur-in-apatite oxybarometer for mafic systems. *Geochimica et*  
916 *Cosmochimica Acta*, 265, 242-258.  
917

- 918 Laurent, A.T., Seydoux-Guillaume, A.-M., Duchene, S., Bingen, B., Bosse, V., and Datas, L.  
919 (2016) Sulphate incorporation in monazite lattice and dating the cycle of sulphur in  
920 metamorphic belts. *Contributions to Mineralogy and Petrology*, 171(11).  
921
- 922 Liu, F., Xu, Z., and Liou, J. (2004) Tracing the boundary between UHP and HP metamorphic  
923 belts in the southwestern Sulu terrane, eastern China: evidence from mineral inclusions in  
924 zircons from metamorphic rocks. *International Geology Review*, 46(5), 409-425.  
925
- 926 Liu, Y., and Comodi, P. (1993) Some aspects of the crystal-chemistry of apatites. *Mineralogical*  
927 *Magazine*, 57(389), 709-719.  
928
- 929 Longerich, H.P., Jackson, S.E., and Günther, D. (1996) Inter-laboratory note. Laser ablation  
930 inductively coupled plasma mass spectrometric transient signal data acquisition and  
931 analyte concentration calculation. *Journal of analytical atomic spectrometry*, 11(9), 899-  
932 904.  
933
- 934 Low, H.R., Phonthammachai, N., Maignan, A., Stewart, G.A., Bastow, T.J., Ma, L.L., and  
935 White, T.J. (2008) The crystal chemistry of ferric oxyhydroxyapatite. *Inorganic*  
936 *Chemistry*, 47(24), 11774-82.  
937
- 938 Manning, C.E. (1994) The solubility of quartz in H<sub>2</sub>O in the lower crust and upper mantle.  
939 *Geochimica et Cosmochimica Acta*, 58(22), 4831-4839.  
940
- 941 Mao, M., Rukhlov, A.S., Rowins, S.M., Spence, J., and Coogan, L.A. (2016) Apatite Trace  
942 Element Compositions: A Robust New Tool for Mineral Exploration. *Economic*  
943 *Geology*, 111(5), 1187-1222.  
944
- 945 Matjuschkin, V., Brooker, R.A., Tattitch, B., Blundy, J.D., and Stamper, C.C. (2015) Control and  
946 monitoring of oxygen fugacity in piston cylinder experiments. *Contributions to*  
947 *Mineralogy and Petrology*, 169(1), 9.  
948
- 949 Migdisov, A., Williams-Jones, A.E., Brugger, J., and Caporuscio, F.A. (2016) Hydrothermal  
950 transport, deposition, and fractionation of the REE: Experimental data and  
951 thermodynamic calculations. *Chemical Geology*, 439, 13-42.  
952
- 953 Moecher, D.P., Anderson, E.D., Cook, C.A., and Mezger, K. (1997) The petrogenesis of  
954 metamorphosed carbonatites in the Grenville Province, Ontario. *Canadian Journal of*  
955 *Earth Sciences*, 34(9), 1185-1201.  
956
- 957 Nash, W.P. (1984) Phosphate Minerals in Terrestrial Igneous and Metamorphic Rocks. In J.O.  
958 Nriagu, and P.B. Moore, Eds. *Phosphate Minerals*, p. 215-241. Springer Berlin  
959 Heidelberg, Berlin, Heidelberg.  
960
- 961 Palma, G., Barra, F., Reich, M., Valencia, V., Simon, A.C., Vervoort, J., Leisen, M., and  
962 Romero, R. (2019) Halogens, trace element concentrations, and Sr-Nd isotopes in apatite  
963 from iron oxide-apatite (IOA) deposits in the Chilean iron belt: Evidence for magmatic



964 and hydrothermal stages of mineralization. *Geochimica et Cosmochimica Acta*, 246, 515-  
965 540.

966

967 Pan, Y., and Fleet, M.E. (2002) Compositions of the Apatite-Group Minerals: Substitution  
968 Mechanisms and Controlling Factors. *Reviews in Mineralogy and Geochemistry*, 48(1),  
969 13-49.

970

971 Parat, F., and Holtz, F. (2004) Sulfur partitioning between apatite and melt and effect of sulfur  
972 on apatite solubility at oxidizing conditions. *Contributions to Mineralogy and Petrology*,  
973 147(2), 201-212.

974

975 Parat, F., and Holtz, F. (2005) Sulfur partition coefficient between apatite and rhyolite: the role  
976 of bulk S content. *Contributions to Mineralogy and Petrology*, 150(6), 643-651.

977

978 Parat, F., Holtz, F., and Feig, S. (2008) Pre-eruptive Conditions of the Huerto Andesite (Fish  
979 Canyon System, San Juan Volcanic Field, Colorado): Influence of Volatiles (C-O-H-S)  
980 on Phase Equilibria and Mineral Composition. *Journal of Petrology*, 49(5), 911-935.

981

982 Parat, F., Holtz, F., and Streck, M.J. (2011) Sulfur-bearing Magmatic Accessory Minerals.  
983 *Reviews in Mineralogy and Geochemistry*, 73(1), 285-314.

984

985 Pasero, M., Kampf, A.R., Ferraris, C., Pekov, I.V., Rakovan, J., and White, T.J. (2010)  
986 Nomenclature of the apatite supergroup minerals. *European Journal of Mineralogy*,  
987 22(2), 163-179.

988

989 Pearson, K. (1895) VII. Note on regression and inheritance in the case of two parents.  
990 *proceedings of the royal society of London*, 58(347-352), 240-242.

991

992 Peng, G., Luhr, J.F., and McGee, J.J. (1997) Factors controlling sulfur concentrations in volcanic  
993 apatite. *American Mineralogist*, 82(11-12), 1210-1224.

994

995 Piccoli, P.M., and Candela, P.A. (2002) Apatite in igneous systems. *Reviews in Mineralogy and*  
996 *Geochemistry*, 48(1), 255-292.

997

998 Putnis, A. (2002) Mineral replacement reactions: from macroscopic observations to microscopic  
999 mechanisms. *Mineralogical Magazine*, 66(5), 689-708.

1000

1001 Putnis, A., Oelkers, E., and Schott, J. (2009) Mineral replacement reactions. *Thermodynamics*  
1002 *and kinetics of water-rock interaction*, 70, 87-124.

1003

1004 Rakovan, J.F., and Hughes, J.M. (2000) STRONTIUM IN THE APATITE STRUCTURE:  
1005 STRONTIAN FLUORAPATITE AND BELOVITE-(Ce). *The Canadian Mineralogist*,  
1006 38(4), 839-845.

1007

1008 Rouse, R.C., and Dunn, P.J. (1982) A contribution to the crystal chemistry of ellestadite and the  
1009 silicate sulfate apatites. *American Mineralogist*, 67(1-2), 90-96.

1010  
1011 Sadove, G., Konecke, B.A., Fiege, A., and Simon, A.C. (2019) Structurally bound S<sup>2-</sup>, S<sup>1-</sup>,  
1012 S<sup>4+</sup>, S<sup>6+</sup> in terrestrial apatite: The redox evolution of hydrothermal fluids at the Phillips  
1013 mine, New York, USA. *Ore Geology Reviews*, 107, 1084-1096.  
1014  
1015 Sallet, R. (2000) Fluorine as a tool in the petrogenesis of quartz-bearing magmatic associations:  
1016 applications of an improved F–OH biotite–apatite thermometer grid. *Lithos*, 50(1-3),  
1017 241-253.  
1018  
1019 Salviulo, G., Bettinelli, M., Russo, U., Speghini, A., and Nodari, L. (2010) Synthesis and  
1020 structural characterization of Fe<sup>3+</sup>-doped calcium hydroxyapatites: role of precursors and  
1021 synthesis method. *Journal of Materials Science*, 46(4), 910-922.  
1022  
1023 Schettler, G., Gottschalk, M., and Harlov, D.E. (2011) A new semi-micro wet chemical method  
1024 for apatite analysis and its application to the crystal chemistry of fluorapatite-chlorapatite  
1025 solid solutions. *American Mineralogist*, 96(1), 138-152.  
1026  
1027 Shannon, R.D. (1976) Revised effective ionic radii and systematic studies of interatomic  
1028 distances in halides and chalcogenides. *Acta Crystallographica Section A*, 32(5), 751-  
1029 767.  
1030  
1031 Spear, F.S., and Pyle, J.M. (2002) Apatite, monazite, and xenotime in metamorphic rocks.  
1032 *Reviews in Mineralogy and Geochemistry*, 48(1), 293-335.  
1033  
1034 Stormer, J.C., Pierson, M.L., and Tacker, R.C. (1993) Variation of F and Cl X-ray intensity due  
1035 to anisotropic diffusion in apatite during electron microprobe analysis. *American*  
1036 *Mineralogist*, 78(5-6), 641-648.  
1037  
1038 Streck, M.J., and Dilles, J.H. (1998) Sulfur evolution of oxidized arc magmas as recorded in  
1039 apatite from a porphyry copper batholith. *Geology*, 26(6), 523-526.  
1040  
1041 Tepper, J.H., and Kuehner, S.M. (1999) Complex zoning in apatite from the Idaho Batholith; a  
1042 record of magma mixing and intracrystalline trace element diffusion. *American*  
1043 *Mineralogist*, 84(4), 581-595.  
1044  
1045 Warner, S., Martin, R.F., Abdel-Rahman, A.-F.M., and Doig, R. (1998) Apatite as a monitor of  
1046 fractionation, degassing, and metamorphism in the Sudbury igneous complex, Ontario.  
1047 *The Canadian Mineralogist*, 36(4), 981-999.  
1048  
1049 Watson, E.B., and Green, T.H. (1981) Apatite/liquid partition coefficients for the rare earth  
1050 elements and strontium. *Earth and Planetary Science Letters*, 56, 405-421.  
1051  
1052 Webster, J.D., and Botcharnikov, R.E. (2011) Distribution of sulfur between melt and fluid in  
1053 SOHC-Cl-bearing magmatic systems at shallow crustal pressures and temperatures.  
1054 *Reviews in Mineralogy and Geochemistry*, 73(1), 247-283.  
1055

- 1056 Webster, J., and Piccoli, P. (2015) Magmatic apatite: a powerful, yet deceptive, mineral.  
1057 Elements, 11, 177–182.  
1058
- 1059 Xiaochun, L. (1993) High-P metamorphic belt in central China and its possible eastward  
1060 extension to Korea. The Journal of the Petrological Society of Korea, 2(1), 9-18.  
1061
- 1062 Zhou, R.-J., Wen, G., Li, J.-W., Jiang, S.-Y., Hu, H., Deng, X.-D., Zhao, X.-F., Yan, D.-R., Wei,  
1063 K.-T., Cai, H.-A., Shang, S.-C., Li, B.-C., and Dai, X.-K. (2022) Apatite chemistry as a  
1064 petrogenetic–metallogenic indicator for skarn ore-related granitoids: an example from the  
1065 Daye Fe–Cu–(Au–Mo–W) district, Eastern China. Contributions to Mineralogy and  
1066 Petrology, 177(2), 23.  
1067
- 1068 Zhu, C., and Sverjensky, D.A. (1991) Partitioning of F-Cl-OH between minerals and  
1069 hydrothermal fluids. Geochimica et Cosmochimica Acta, 55(7), 1837-1858.  
1070
- 1071

1072

### List of In Text Figure Captions

1073 **Figure 1:** BSE image of a representative grain of the starting synthetic fluorapatite (APS 102).

1074 Starting synthetic fluorapatite grains are euhedral, elongate, and homogenous in BSE image  
1075 grayscale. Scale bar represents 170  $\mu\text{m}$ .

1076

1077 **Figure 2:** **a)** High-contrast BSE image of a grain from experiment FS12. Grains are subhedral to

1078 anhedral, slightly rounded, exhibit a subtle greyscale zonation with diffuse boundaries. The red

1079 arrow indicates traces of beam damage visible in the BSE and CL images. **b)** Diffuse zonation in

1080 monochromatic CL image. **c-f)** Wavelength dispersive spectroscopy elemental maps of spatially

1081 correlated Na, Si, S, and F. Note the diffuse zonation boundaries for F. **g)** Atoms per formula

1082 unit (a.p.f.u.) scatter plot where red symbols compare S on the x-axis and Na on the y-axis, and

1083 blue symbols compare S on the x-axis and Si on the y-axis. Error bars represent X-ray counting

1084 error and can be smaller than the symbols. Detection limits are indicated by dashed lines. The 1:1

1085 line represents the sulfate coupled substitutions from Equations 1 and 2.

1086

1087 **Figure 3:** **a)** High-contrast BSE image of a grain from experiment FS11. Grain is anhedral and

1088 slightly rounded with partially healed fractures. **b)** Distinct zonation boundary in monochromatic

1089 CL image. **c-f)** Wavelength dispersive spectroscopy elemental maps of Si and F, and spatially

1090 correlated Na and S. **g)** Atoms per formula unit (a.p.f.u.) scatter plot where red symbols compare

1091 S on the x-axis and Na on the y-axis, and blue symbols compare S on the x-axis and Si on the y-

1092 axis. Error bars represent X-ray counting error and can be smaller than the symbols. Detection

1093 limits are indicated by dashed lines. The 1:1 line represents the sulfate coupled substitutions

1094 from Equations 1 and 2.

1095

1096

1097 **Figure 4: a)** High-contrast BSE image of a grain from experiment FS9. Grains are subhedral to  
1098 anhedral and homogenous in high-contrast BSE image grayscale. **b)** Monochromatic CL image  
1099 of representative grain. Grid pattern is artifact of data processing. **c-f)** Wavelength dispersive  
1100 spectroscopy elemental maps of Na, Fe, S, and Cl. A positive spatial correlation is visible for Fe,  
1101 S, and Cl. Note the diffuse zonation of Cl. **g)** Atoms per formula unit (a.p.f.u.) scatter plot where  
1102 red symbols compare S on the x-axis and Na on the y-axis, and blue symbols compare S on the  
1103 x-axis and Si on the y-axis. The 1:1 line represents the sulfate coupled substitutions from  
1104 Equations 1 and 2. **h)** Atoms per formula unit (a.p.f.u.) scatter plot where red symbols compare S  
1105 on the x-axis and Fe on the y-axis. Error bars for a.p.f.u. scatter plots represent X-ray counting  
1106 error and can be smaller than the symbols. Detection limits are indicated by dashed lines. Black  
1107 square indicates cluster with independent Fe and S concentrations. Dashed red line indicates  
1108 approximate trend of data points for the proposed  $\text{Fe}^{3+} + \text{S}^{4+} = \text{Ca}^{2+} + \text{P}^{5+}$  coupled substitution.

1109

1110 **Figure 5: a)** High-contrast BSE image of a grain from experiment FS10. Grains are euhedral to  
1111 anhedral with a bi-modal grayscale in high-contrast BSE imagery where darker, inclusion-free  
1112 regions are marked by a sharp reaction front traced by micrometer to sub-micrometer scale bright  
1113 monazite-(Ce) inclusions (Mnz) that separate brighter regions with numerous  $\leq 5 \mu\text{m}$  inclusions.  
1114 **b)** Monochromatic CL image of representative grain. Negative black regions are an artifact from  
1115 non-optimized brightness/contrast settings during automated electron microprobe data collection.  
1116 **c-f)** Wavelength dispersive spectroscopy elemental maps of distinctly zoned Ce and S, and Na  
1117 and Si that exhibit subtle zoning. Cerium and S exhibit strong positive spatial correlation with a

1118 more subtle Na and Si spatial correlation. **g)** Atoms per formula unit (a.p.f.u.) scatter plot where  
1119 red symbols are S vs. Na on the y-axis and blue symbols are S vs. Si on the y-axis for analyses of  
1120 the darker regions visible in BSE grayscale. Green symbols are S vs. Na on the y-axis and purple  
1121 symbols are S vs. Si on the y-axis for analyses of the brighter regions visible in BSE grayscale.  
1122 The 1:1 line represents the sulfate coupled substitutions from Equations 1 and 2. **h)** Atoms per  
1123 formula unit (a.p.f.u.) scatter plot where blue symbols are S vs. Ce for the BSE-dark regions and  
1124 red symbols are S vs. Ce for the BSE-bright regions. Error bars for a.p.f.u. scatter plots represent  
1125 the X-ray counting error and can be smaller than the symbols. Detection limits are indicated by  
1126 dashed lines.

1127

1128 **Figure 6: a)** High-contrast BSE image of a grain from experiment FS14. The red dashed line is  
1129 the approximate location of the apatite grain boundary. Grains are subhedral to anhedral with a  
1130 bi-modal grayscale in high-contrast BSE imagery where the brighter regions are mantling darker  
1131 cores. Fluorapatite grains are sometimes mantled by masses of Cl-rich SrSO<sub>4</sub>. **b)** Monochromatic  
1132 CL image of representative grain where CL brightness presents inverse to BSE image intensity.  
1133 The red dashed line is the approximate location of the apatite grain boundary. **c-f)** Wavelength  
1134 dispersive spectroscopy elemental maps of Na, S, Sr, and Si. Sodium, S, and Sr exhibit a strong  
1135 positive correlation in the zoned apatite. The bright green dashed line in (c) is the approximate  
1136 location of the apatite grain boundary. **g)** Atoms per formula unit (a.p.f.u.) scatter plot where red  
1137 symbols are S vs. Na on the y-axis and blue symbols are S vs. Si on the y-axis for analyses of the  
1138 darker regions visible in BSE grayscale. Green symbols are S vs. Na on the y-axis and purple  
1139 symbols are S vs. Si on the y-axis for analyses of the brighter regions visible in BSE grayscale.  
1140 The 1:1 line represents the sulfate coupled substitutions from Equations 1 and 2. Error bars for

1141 a.p.f.u. scatter plots represent X-ray counting error and are smaller than the symbols. Detection  
1142 limits are indicated by dashed lines.

1143

1144 **Figure 7: a)** High-contrast BSE image of a grain from experiment FS6-2. Grains are anhedral  
1145 and exhibit numerous, subparallel, dissolution pits that extend into the grain. Two regions are  
1146 visible in high-contrast BSE imagery, a darker homogenous core that shares a distinct reaction  
1147 front with brighter grain margins. The brighter grain margins exhibit a heterogenous grayscale on  
1148 the micrometer scale with a combination of distinct and diffuse reaction fronts. **b)**  
1149 Monochromatic CL image of representative grain where CL brightness presents inverse to BSE  
1150 image intensity. **c-f)** Wavelength dispersive spectroscopy elemental maps of Fe, S, Si, and F.  
1151 Iron and S exhibit a strong positive spatial correlation in the zoned apatite. **g)** Atoms per formula  
1152 unit (a.p.f.u.) scatter plot where red symbols are S vs. Na on the y-axis and blue symbols are S  
1153 vs. Si on the y-axis for analyses of the darker regions visible in BSE grayscale. Green symbols  
1154 are S vs. Na on the y-axis and purple symbols are S vs. Si on the y-axis for analyses of the  
1155 brighter regions visible in BSE grayscale. The 1:1 line represents the sulfate coupled  
1156 substitutions from Equations 1 and 2. **h)** Atoms per formula unit (a.p.f.u.) scatter plot where blue  
1157 symbols are S vs. Fe for the darker BSE regions and yellow symbols are S vs. Fe for the brighter  
1158 BSE regions. Error bars for a.p.f.u. scatter plots represent X-ray counting error and can be  
1159 smaller than the symbols. Detection limits are indicated by dashed lines.

1160

1161 **Figure 8: a)** Atoms per formula unit (a.p.f.u.) scatter plot where red circles represent S and Na  
1162 concentrations for all S-bearing run products, the black X-symbols are representative of reported  
1163 S and Na concentrations in metamorphic apatite grains (Liu and Comodi, 1993; Warner et al.,

1164 1998; Harlov et al., 2002b), the inverted black triangles are representative of reported S and Na  
1165 concentrations in the Mina Carmen apatite grains (Palma et al., 2019), and the grey polygon with  
1166 the dashed outline is the approximate region of reported S and Na concentrations in apatite  
1167 grains from apatite-melt partition experiments (modified from Parat et al., 2011; references  
1168 therein). **b)** Atoms per formula unit (a.p.f.u.) scatter plot where open circles represent the ‘low S’  
1169 concentration experiments FS3 and FS20, the open squares represent the ‘moderate S’  
1170 concentration experiments FS8 and FS15, the blue symbols represent experiments FS12 and  
1171 FS13 that plot on or near the 1:1 atomic ratio line, the black X-symbols are representative of  
1172 reported S and Si concentrations in metamorphic apatite grains (Liu and Comodi, 1993; Warner  
1173 et al., 1998; Harlov et al., 2002b), the inverted black triangles are representative of reported S  
1174 and Si concentrations in the Mina Carmen apatite grains (Palma et al., 2019), and the grey  
1175 polygon with the dashed outline is the approximate region of reported S and Si concentrations in  
1176 apatite grains from apatite-melt partition experiments (modified from Parat et al., 2011;  
1177 references therein). The 1:1 line represents the ideal sulfate coupled substitutions from Equations  
1178 1 and 2.

1179

1180 **Figure 9:** Ternary plot illustrating F-Cl-OH halogen site occupancy in percent for experiment  
1181 run products assessing the effects of halogen site chemistry on S incorporation and the starting  
1182 synthetic apatite grains (APS-102). The chemical formula for run products is calculated using 5  
1183 cations and 26 oxygens; assuming that the halogen site (X) is occupied by F, Cl, OH and that the  
1184 S present in the fluorapatite is oxidized and occupies the tetrahedral site (T).

1185

1186

### List of Supplementary Figure Captions



1187 **Supplementary Figure 1:** BSE images of representative fluorapatite grains from experiments  
1188 where average S concentrations are below electron microprobe (EMP) detection limits. **a)**  
1189 Representative grain from experiment FS1. Run-product apatite grains are homogenous in BSE  
1190 image grayscale, subhedral to anhedral, with few rounded grain margins. **b)** Representative grain  
1191 from experiment FS2. Run-product apatite grains are homogenous in BSE image grayscale,  
1192 dominantly anhedral, and occasionally fractured. **c)** Representative grain from experiment FS3.  
1193 Grains are homogenous in BSE image grayscale, subhedral to anhedral, slightly rounded, and  
1194 occasionally mantled by a silicate glass that was not analyzed for its chemical composition.  
1195 Brighter spots, indicated by a red arrow, on apatite grain are beam damage from EMP analyses.  
1196 **d)** Representative grain from experiment FS4. Grains are homogenous in BSE image grayscale,  
1197 subhedral to anhedral, slightly rounded from dissolution, with sub-micrometer monazite (Mnz)  
1198 grains found in partially healed fractures and mantling the fluorapatite (Ap) grains. Brighter  
1199 spots, indicated by a red arrow, on apatite grain are beam damage from EMP analyses. **e)**  
1200 Representative grain from experiment FS7. Grains are homogenous in BSE image grayscale and  
1201 anhedral with slightly concave margins from conchoidal fracturing. **f)** Representative grain from  
1202 experiment FS16. Grains are homogenous in BSE image grayscale, and subhedral to anhedral  
1203 with partially healed fractures. **g)** Representative grain from experiment FS20. Grains of  
1204 fluorapatite (Ap) are homogenous in BSE image grayscale, subhedral to anhedral, with shallow  
1205 etch pits, and occasional subtle rounding of corners. Aggregate masses of small ( $\leq 50 \mu\text{m}$ )  
1206 euhedral to subhedral secondary quartz grains (Si) are present but were not analyzed for their  
1207 chemical composition. Brighter spots, indicated by a red arrow, on apatite grain are beam  
1208 damage from EMP analyses. **h)** Representative grain from experiment FS21. Grains of  
1209 fluorapatite (Ap) are homogenous in BSE image grayscale, and subhedral to anhedral with subtle

1210 rounding of corners. Sub-micrometer monazite-(Ce) (Mnz) grains can be found filling fractures.  
1211 Brighter spots, indicated by a red arrow, on apatite grain are beam damage from EMP analyses.

1212

1213 **Supplementary Figure 2: a)** High-contrast BSE image of a grain from experiment FS15. Grains  
1214 are euhedral to anhedral, slightly rounded and exhibit a subtle greyscale zonation. White dashed  
1215 line indicates approximate location of zonation boundary between overgrowth and seed crystal.  
1216 **b)** diffuse boundary zonation in monochromatic CL image. **c-f)** Wavelength dispersive  
1217 spectroscopy elemental maps of spatially correlated Na, Si, S, and F. Note the distinct zonation  
1218 boundary for Na and S, and the diffuse boundary for F. Bright spots in Na and Si map are Na-Si  
1219 glass spheroids. **g)** Atoms per formula unit (a.p.f.u.) scatter plot where red symbols compare S on  
1220 the x-axis and Na on the y-axis, and blue symbols compare S on the x-axis and Si on the y-axis.  
1221 Error bars represent X-ray counting error and can be smaller than the symbols. Detection limits  
1222 are indicated by dashed lines. The 1:1 line represents the sulfate coupled substitutions from  
1223 Equations 1 and 2.

1224

1225 **Supplementary Figure 3: a)** High-contrast BSE image of a grain from experiment FS8. Grains  
1226 are euhedral to anhedral, slightly rounded and homogenous in BSE grayscale. Bright spots on the  
1227 apatite grain are beam damage from previous analyses. **b)** Monochromatic CL image with no  
1228 apparent zonation. Beam damage visible as dark spots. **c-f)** Wavelength dispersive spectroscopy  
1229 elemental maps of spatially correlated Na, Si, S, and Cl. Note the distinct zonation boundary for  
1230 S and the diffuse boundary for Cl. Bright spots in Si map are silicate glass spheroids. **g)** Atoms  
1231 per formula unit (a.p.f.u.) scatter plot where red symbols compare S on the x-axis and Na on the  
1232 y-axis, and blue symbols compare S on the x-axis and Si on the y-axis. Error bars represent X-

1233 ray counting error and can be smaller than the symbols. Detection limits are indicated by dashed  
1234 lines. The 1:1 line represents the sulfate coupled substitutions from Equations 1 and 2.

1235  
1236 **Supplementary Figure 4: a)** High-contrast BSE image of fluorapatite grain (Ap) from  
1237 experiment FS13. Grains are subhedral to anhedral and homogenous in BSE image grayscale.  
1238 Elongate grains of accessory wollastonite (Wol) and spheroids of sodium silicate glass (Na-Si)  
1239 are present but were not analyzed for their chemical compositions. Dashed white line indicates  
1240 approximate c-axis orientation. Bright spots on the apatite grain are from electron beam damage.  
1241 **b)** Distinct zonation boundaries in monochromatic CL imagery. **c-f)** Wavelength dispersive  
1242 spectroscopy elemental maps of Cl and spatially correlated Na, Si, and S. **g)** Atoms per formula  
1243 unit (a.p.f.u.) scatter plot where red symbols compare S on the x-axis and Na on the y-axis, and  
1244 blue symbols compare S on the x-axis and Si on the y-axis. Error bars represent X-ray counting  
1245 error are smaller than the symbols. Detection limits are indicated by dashed lines. The 1:1 line  
1246 represents the sulfate coupled substitutions from Equations 1 and 2.

1247  
1248 **Supplementary Figure 5: a)** High-contrast BSE image of a grain from experiment FS17. Grains  
1249 are dominantly subhedral to anhedral with partially healed fractures, and larger masses ( $> 100$   
1250  $\mu\text{m}$ ) of smaller ( $\leq 15\mu\text{m}$ ) grain aggregates. Grains are euhedral to subhedral and exhibit grain to  
1251 grain variation in BSE images. **b)** Subtle zonation in monochromatic CL imagery. **c-f)**  
1252 Wavelength dispersive spectroscopy elemental maps of spatially correlated Na and S, and  
1253 inversely correlated F and Cl. **g)** Atoms per formula unit (a.p.f.u.) scatter plot where red symbols  
1254 compare S on the x-axis and Na on the y-axis, and blue symbols compare S on the x-axis and Si  
1255 on the y-axis. Error bars represent X-ray counting error are smaller than the symbols. Detection

1256 limits are indicated by dashed lines. The 1:1 line represents the sulfate coupled substitutions  
1257 from Equations 1 and 2.

**Table 1. Summary of experimental results**

Experiment	P (GPa)	T(°C)	Time (days)	Synthetic fluorapatite	H <sub>2</sub> O	1M H <sub>2</sub> SO <sub>4</sub>	Na <sub>2</sub> SO <sub>4</sub>	FeCl <sub>3</sub>	SrCl <sub>2</sub>	CeCl <sub>3</sub>	SiO <sub>2</sub>
FS1	1	800	5	19.12		5.16		5.5			
FS2	1	800	5	19.28	4.95		4.3				
FS3	1	800	5	20.14		4.88					4.4
FS4	1	800	5	20.3		5.01				4.2	
FS6-2	1	800	8 hrs.	20.6	5.98						
FS7	1	800	5	20.96	5.72		5.03				
FS8	1	800	5	21.21		5.39					5.91
FS9	1	800	5	19.45		5.59		4.96			
FS10	1	800	5	21.14		5.37				5.06	
FS11	1	800	5	22.6	5.73		6.01				
FS12	1	800	5	20.18	5.84		5.21				
FS13	1	800	5	20.2	5.98		6.73				
FS14	1	800	5	20.32	5.18		5.97		6.52		
FS15	1	800	5	6.41	5.15		2.63				1.42
FS16	1	800	5	20.16	6.03		6.38				
FS17	1	800	5	19.56	5.97		5.38				
FS20	1	800	5	20.7	5.06		5.19				5.45
FS21	1	800	5	19.81	5.52		5.45			5.38	

Solids and liquids in mg. In high contrast BSE images of run products: all grains from a single experiment are equivalent in grayscale intensity and

Na <sub>2</sub> Si <sub>2</sub> O <sub>5</sub>	β-Ca <sub>3</sub> (PO <sub>4</sub> ) <sub>2</sub>	FeS	CaCl <sub>2</sub>	NaF	Ca(OH) <sub>2</sub>	Initial Wt.% S*	Initial Wt.% Cl*	Results
						4.4	11.3	Run product apatite grains are sub-hedral to anhedral, with fe
						10.5		Run product apatite grains are occasionally fractured and dor
						4.8		Run product apatite grains are slightly rounded and sub-hedra
						4.9	6.6	Run product apatite grains are sub-hedral to anhedral and slig mantling fluorapatite grains.
	9.45					22.3		Run product apatite grains are anhedral, have numerous sub-p contrast BSE images. Sharp reaction front is visible in gray sc Reprecipitated fluorapatite on rims are sometimes faceted.
			5.1			7.2	10.3	Run product apatite grains are anhedral with slightly concave
			5.17			3.0	10.0	Run product apatite grains are anhedral, dominantly rounded i
			5.16			3.2	17.4	Run product apatite grains are sub-hedral to anhedral, with ag
			5.45			3.1	15.5	Run product apatite grains are euhedral to anhedral, with num show a bi-modal grayscale; darker, inclusion free, regions anc front.
				1.92		9.9		Run product apatite grains are sub-hedral to anhedral, are slig
7.35						6.4		Run product apatite grains are sub-hedral to anhedral and are
8.23			2.74			6.4	3.7	Run product apatite grains are sub-hedral to anhedral with ag fluorapatite grains, including aggregates, are homogenous in ξ
						7.6	8.3	Run product apatite grains are sub-hedral to anhedral with a b the darker grains. Brighter regions sometimes exhibit subtle a
	11.22			0.95		2.8		Run product apatite grains are euhedral to anhedral, 10s to 10 mantled by aggregates of smaller grains that have grown toge
					5.38	8.1		Run product apatite grains are sub-hedral to anhedral, with pa
			5.37		5.05	5.6	7.9	Run product apatite grains are dominantly sub-hedral to anhe (≤15μm) euhedral to sub-hedral grains.
			5.77			5.5	8.6	Run product apatite grains are sub-hedral to anhedral, concav aggregate masses of small (≤50μm) euhedral to sub-hedral sec
			4.73			5.8	10.8	Run product apatite grains are sub-hedral to anhedral with sut little evidence of fluorapatite dissolution.

† individual grains are homogenous in grayscale, unless otherwise noted. \* = wt.% of element relative to total mass of starting liquid and reagents.

---

w lobate margins.

inantly anhedral.

l to anhedral. Fluorapatite is occasionally mantled by silicate glass.

htly rounded from dissolution reprecipitation. Sub-micron monazite grains are found in partially healed fractures and

parallel dissolution pits 5-20  $\mu\text{m}$  deep that extend into the grain, with minor 5  $\mu\text{m}$  or less bright iron sulfide grains in high  
scale of BSE images separating darker cores from brighter rims; dissolution pits do not extend into darker cores.

margins from conchoidal fracturing.

margins with occasional facets.

gregates of sub-hedral grains overgrown by larger anhedral masses.

erous  $\leq 5 \mu\text{m}$  Monazite-(Ce) inclusions and/or grains mantling the fluorapatite. In high contrast BSE images, some grains  
l a sharp reaction front separating brighter regions. Micron to sub-micron scale monazite inclusions trace the reaction

htly rounded with partially healed fractures.

slightly rounded.

gregates of smaller ( $\leq 15 \mu\text{m}$ ) grains growing together to form larger anhedral grains. In high contrast BSE images the  
grayscale. Elongate grains of accessory Wollastonite and spheroids of sodium silicate glass are present.

i-modal grayscale in high contrast BSE images. Brighter regions are found mantling darker cores and filling fractures of  
nd/or sharp zonation in grayscale. Few fluorapatite grains are mantled by large ( $>200 \mu\text{m}$ ) masses of Cl rich  $\text{SrSO}_4$ .

0s of microns across, and present a homogenous grayscale in high contrast BSE images. Fluorapatite seed grains are  
ther and have an indiscernible boundary with the seed crystals.

rtially healed fractures, and clusters of small ( $\leq 15 \mu\text{m}$ ) fluorapatite grains found on rims of larger grains.

dral with partially healed fractures, and occasionally larger grains ( $>100 \mu\text{m}$ ) are comprised of aggregates of smaller

e grain margins from conchoidal fracturing, and occasionally subtle rounding of corners. Large ( $>300 \mu\text{m}$ ) elongate  
condary quartz grains.

otle rounding of corners. Sub-micron monazite-(Ce) grains can be found filling fractures of fluorapatite grains despite

---

---

**Table 2. Chemical composition of run products from EPMA analyses**

Exp	P (MPa)	T (°C)	time	area	# pts.	P (%)	Si (µg/g)	S (µg/g)	Ce (%)	Ca (%)	Fe (%)	Sr (%)	Na (%)	F (%)	Cl (%)
Synthetic fluorapatite used in this study					65	18.54 <i>0.01</i>	38 <i>1</i>			39.14 <i>0.05</i>		0.02 <i>0.00</i>	0.02 <i>0.00</i>	3.70 <i>0.01</i>	0.01 <i>0.00</i>
FS1	1000	800	5 days		42	18.53 <i>0.02</i>	51 <i>2</i>			39.19 <i>0.04</i>		0.03 <i>0.00</i>	0.02 <i>0.00</i>	3.74 <i>0.03</i>	0.01 <i>0.00</i>
FS2	1000	800	5 days		56	18.32 <i>0.01</i>	62 <i>2</i>			39.51 <i>0.04</i>		0.03 <i>0.00</i>	0.01 <i>0.00</i>	3.60 <i>0.03</i>	
FS3	1000	800	5 days		34	18.53 <i>0.02</i>	53 <i>3</i>			39.49 <i>0.06</i>		0.03 <i>0.00</i>	0.02 <i>0.00</i>	3.64 <i>0.04</i>	
FS4	1000	800	5 days		18	18.35 <i>0.05</i>	54 <i>3</i>			39.16 <i>0.09</i>		0.02 <i>0.00</i>	0.02 <i>0.00</i>	3.62 <i>0.05</i>	0.07 <i>0.02</i>
FS6-2	1000	800	8 hrs.	dark	30	18.40 <i>0.03</i>	57 <i>2</i>	71 <i>4</i>		39.26 <i>0.06</i>		0.03 <i>0.00</i>		3.65 <i>0.03</i>	
				light	4	18.03 <i>0.07</i>	44 <i>4</i>	461 <i>103</i>		37.47 <i>0.72</i>	2.45 <i>0.81</i>	0.01 <i>0.00</i>	0.01 <i>0.00</i>	3.58 <i>0.17</i>	
FS7	1000	800	5 days		40	18.42 <i>0.02</i>	56 <i>2</i>			39.66 <i>0.05</i>		0.03 <i>0.00</i>	0.02 <i>0.00</i>	3.52 <i>0.04</i>	0.01 <i>0.00</i>
FS8	1000	800	5 days		30	18.29 <i>0.02</i>	43 <i>2</i>	105 <i>21</i>		39.16 <i>0.04</i>		0.02 <i>0.00</i>	0.03 <i>0.00</i>	3.40 <i>0.04</i>	0.44 <i>0.07</i>
FS9	1000	800	5 days		27	18.16 <i>0.03</i>	48 <i>4</i>	154 <i>26</i>		39.16 <i>0.05</i>	0.09 <i>0.01</i>	0.02 <i>0.00</i>	0.03 <i>0.00</i>	3.34 <i>0.06</i>	0.58 <i>0.06</i>
FS10	1000	800	5 days	dark	24	18.32 <i>0.03</i>	48 <i>3</i>		0.34 <i>0.15</i>	39.22 <i>0.12</i>		0.02 <i>0.00</i>	0.03 <i>0.00</i>	3.43 <i>0.05</i>	0.48 <i>0.06</i>
				light	14	18.11 <i>0.13</i>	39 <i>6</i>	153 <i>58</i>	2.03 <i>1.32</i>	37.93 <i>0.89</i>		0.02 <i>0.00</i>	0.03 <i>0.00</i>	3.18 <i>0.08</i>	0.83 <i>0.06</i>
FS11	1000	800	5 days		32	18.24 <i>0.03</i>	68 <i>2</i>	452 <i>53</i>		39.74 <i>0.08</i>		0.03 <i>0.00</i>	0.07 <i>0.00</i>	3.63 <i>0.03</i>	
FS12	1000	800	5 days		52	18.22 <i>0.03</i>	228 <i>28</i>	347 <i>57</i>		39.22 <i>0.05</i>		0.03 <i>0.00</i>	0.03 <i>0.00</i>	3.22 <i>0.07</i>	
FS13	1000	800	5 days		21	18.21 <i>0.06</i>	440 <i>153</i>	416 <i>176</i>		39.14 <i>0.09</i>		0.04 <i>0.00</i>	0.02 <i>0.01</i>	3.34 <i>0.12</i>	0.01 <i>0.00</i>
FS14	1000	800	5 days	dark	41	18.52 <i>0.02</i>	47 <i>2</i>			39.26 <i>0.05</i>		0.02 <i>0.00</i>	0.03 <i>0.00</i>	3.66 <i>0.03</i>	0.01 <i>0.00</i>
				light	15	17.17 <i>0.06</i>	59 <i>3</i>	3514 <i>87</i>		32.30 <i>0.25</i>		10.24 <i>0.39</i>	0.20 <i>0.00</i>	3.29 <i>0.03</i>	0.09 <i>0.01</i>
FS15	1000	800	5 days		53	18.43 <i>0.02</i>	55 <i>2</i>	436 <i>43</i>		39.34 <i>0.05</i>		0.03 <i>0.00</i>	0.07 <i>0.00</i>	3.71 <i>0.02</i>	0.01 <i>0.00</i>
FS16	1000	800	5 days		20	18.35 <i>0.03</i>	46 <i>2</i>			39.78 <i>0.09</i>		0.02 <i>0.00</i>	0.02 <i>0.00</i>	3.64 <i>0.08</i>	
FS17	1000	800	5 days		31	18.22 <i>0.03</i>	39 <i>10</i>	156 <i>98</i>		39.38 <i>0.05</i>		0.02 <i>0.00</i>	0.03 <i>0.00</i>	3.21 <i>0.15</i>	0.03 <i>0.01</i>
FS20	1000	800	5 days		30	18.37	40			39.09		0.02	0.01	3.64	0.01



					<i>0.02</i>	3	<i>0.04</i>	<i>0.00</i>	<i>0.00</i>	<i>0.03</i>	<i>0.00</i>
FS21	1000	800	5 days	38	18.32		39.73	0.03		3.65	0.04
					<i>0.02</i>		<i>0.05</i>	<i>0.00</i>		<i>0.03</i>	<i>0.01</i>

---

Standard error ( $1/\sqrt{n}$ ) in *italics*. Blank = below EPMA detection limit. \* = calculated from EPMA data. † = site vacancy.

---

O* (%)	Sum (%)	est. OH* (%)	F	Cl	OH
38.02 <i>0.03</i>	99.46		1.90 <i>0.01</i>	0.00 <i>0.00</i>	0.10 <sup>†</sup> <i>0.01</i>
38.01 <i>0.03</i>	99.53	0.15	1.91 <i>0.01</i>	0.00 <i>0.00</i>	0.08 <i>0.01</i>
37.95 <i>0.03</i>	99.45	0.25	1.85 <i>0.02</i>		0.14 <i>0.02</i>
38.18 <i>0.04</i>	99.90	0.24	1.86 <i>0.02</i>		0.14 <i>0.02</i>
37.81 <i>0.06</i>	99.06	0.21	1.86 <i>0.02</i>	0.02 <i>0.01</i>	0.12 <i>0.02</i>
37.93 <i>0.04</i>	99.30	0.21	1.88 <i>0.01</i>		0.12 <i>0.01</i>
37.52 <i>0.16</i>	99.11	0.24	1.86 <i>0.08</i>		0.14 <i>0.08</i>
38.15 <i>0.04</i>	99.81	0.32	1.81 <i>0.02</i>	0.00 <i>0.00</i>	0.19 <i>0.02</i>
37.76 <i>0.04</i>	99.12	0.21	1.76 <i>0.02</i>	0.12 <i>0.02</i>	0.12 <i>0.02</i>
37.62 <i>0.04</i>	99.03	0.20	1.73 <i>0.03</i>	0.16 <i>0.02</i>	0.11 <i>0.02</i>
37.85 <i>0.06</i>	99.70	0.18	1.76 <i>0.02</i>	0.13 <i>0.02</i>	0.10 <i>0.02</i>
37.39 <i>0.27</i>	99.54	0.19	1.66 <i>0.03</i>	0.23 <i>0.02</i>	0.11 <i>0.02</i>
38.00 <i>0.04</i>	99.78	0.23	1.87 <i>0.01</i>		0.13 <i>0.01</i>
37.93 <i>0.04</i>	98.72	0.55	1.68 <i>0.04</i>		0.32 <i>0.04</i>
37.86 <i>0.06</i>	98.71	0.46	1.73 <i>0.06</i>	0.00 <i>0.00</i>	0.26 <i>0.06</i>
38.07 <i>0.04</i>	99.59	0.21	1.88 <i>0.01</i>	0.00 <i>0.00</i>	0.12 <i>0.01</i>
36.14 <i>0.09</i>	99.79	0.31	1.78 <i>0.01</i>	0.03 <i>0.00</i>	0.19 <i>0.01</i>
38.05 <i>0.03</i>	99.69	0.17	1.90 <i>0.01</i>	0.00 <i>0.00</i>	0.10 <i>0.01</i>
38.06 <i>0.06</i>	99.89	0.24	1.87 <i>0.04</i>		0.13 <i>0.04</i>
37.93 <i>0.06</i>	98.84	0.56	1.66 <i>0.08</i>	0.01 <i>0.00</i>	0.33 <i>0.07</i>
37.80	98.95	0.20	1.88	0.00	0.11

<i>0.03</i>			<i>0.01</i>	<i>0.00</i>	<i>0.01</i>
<i>37.99</i>	<i>99.78</i>	<i>0.20</i>	<i>1.88</i>	<i>0.01</i>	<i>0.11</i>
<i>0.04</i>			<i>0.01</i>	<i>0.00</i>	<i>0.01</i>

---

---

Figure 1

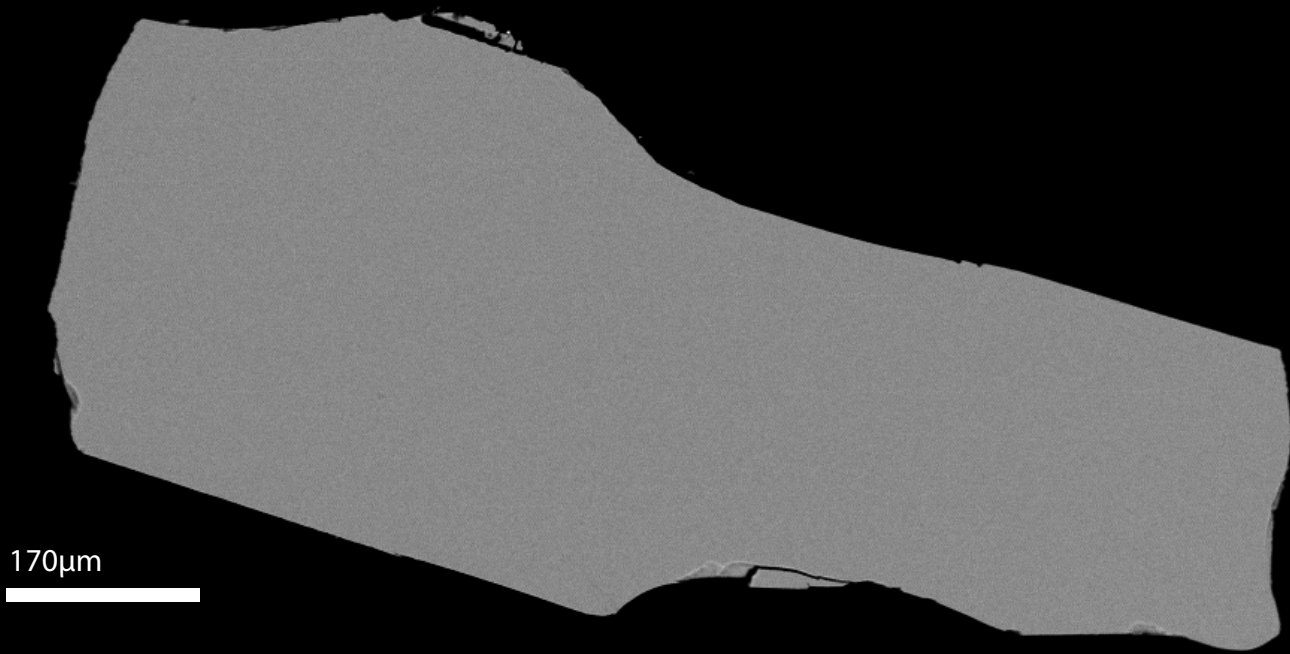


Figure 2

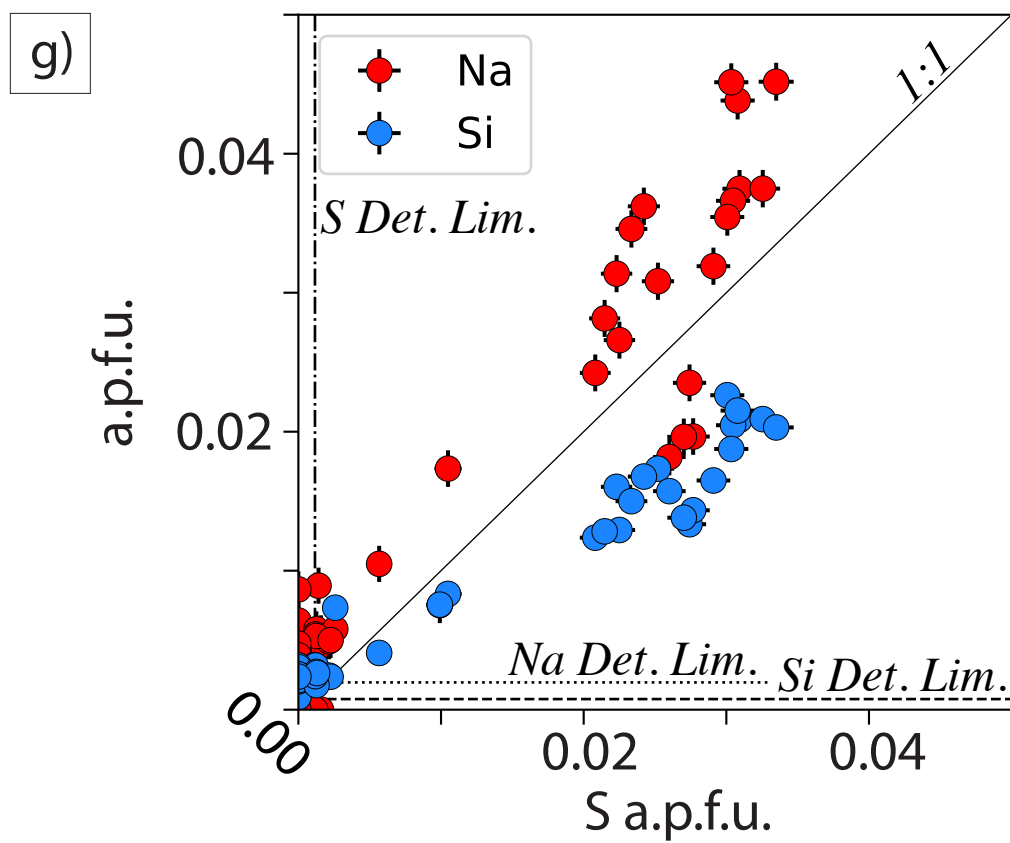
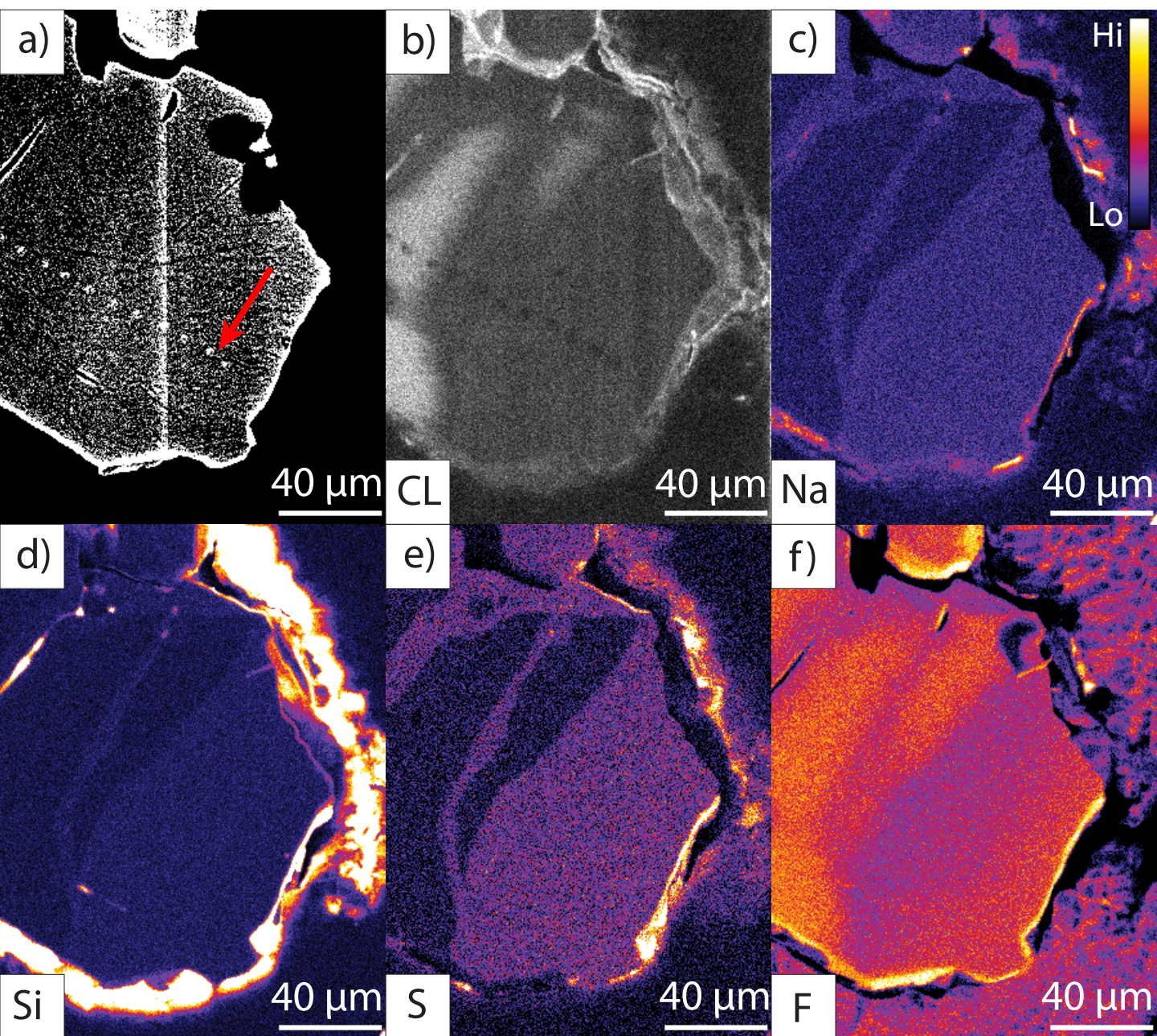




Figure 3

FS11: FIAP + Na<sub>2</sub>SO<sub>4</sub> + NaF + H<sub>2</sub>O

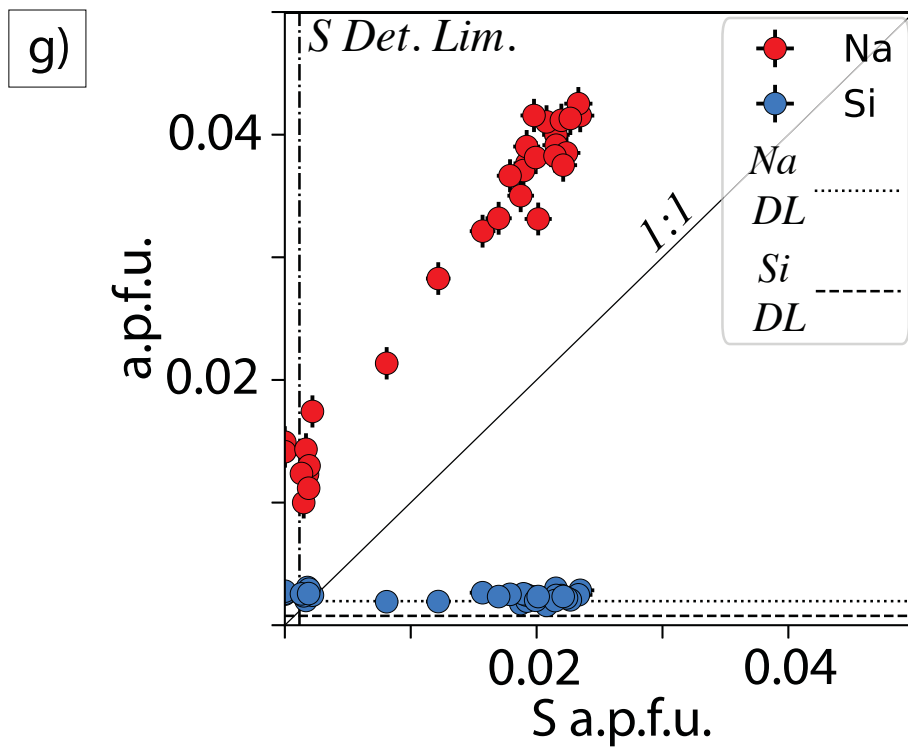
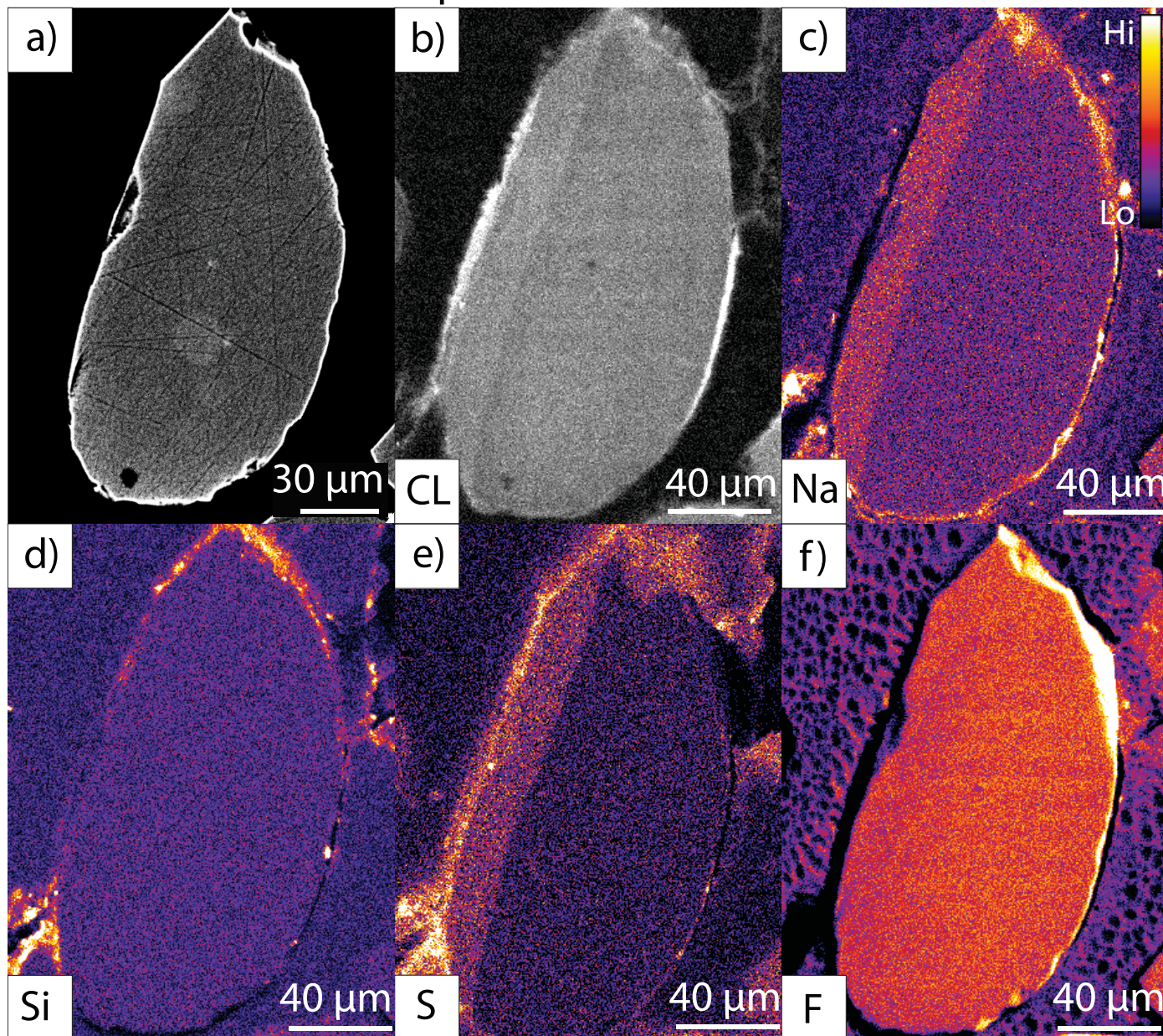




Figure 4

FS9: FlAp + 1M H<sub>2</sub>SO<sub>4</sub> + FeCl<sub>3</sub> + CaCl<sub>2</sub> + H<sub>2</sub>O

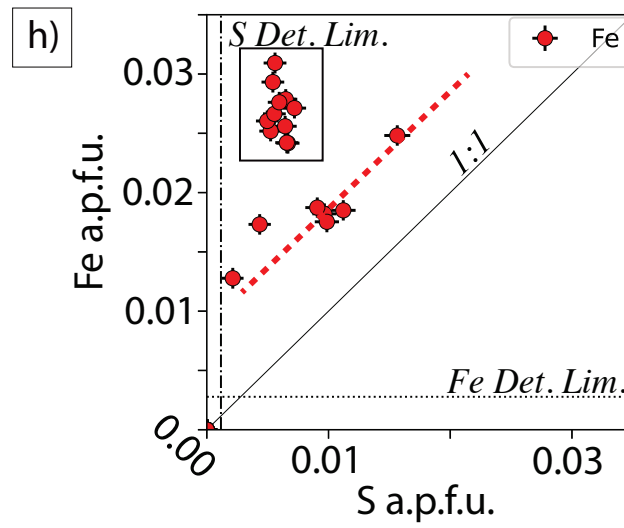
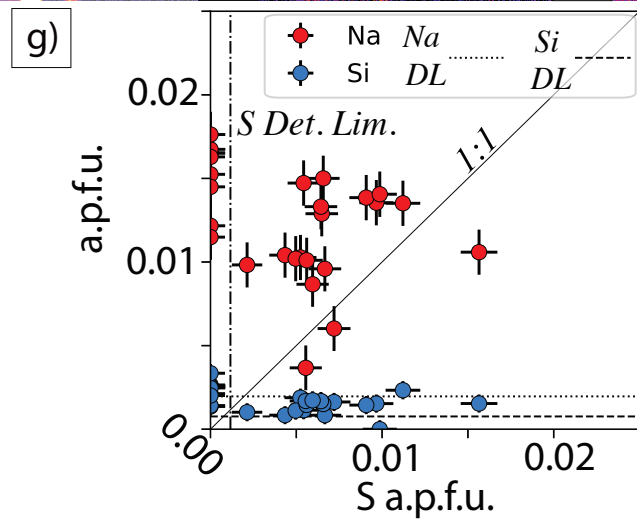
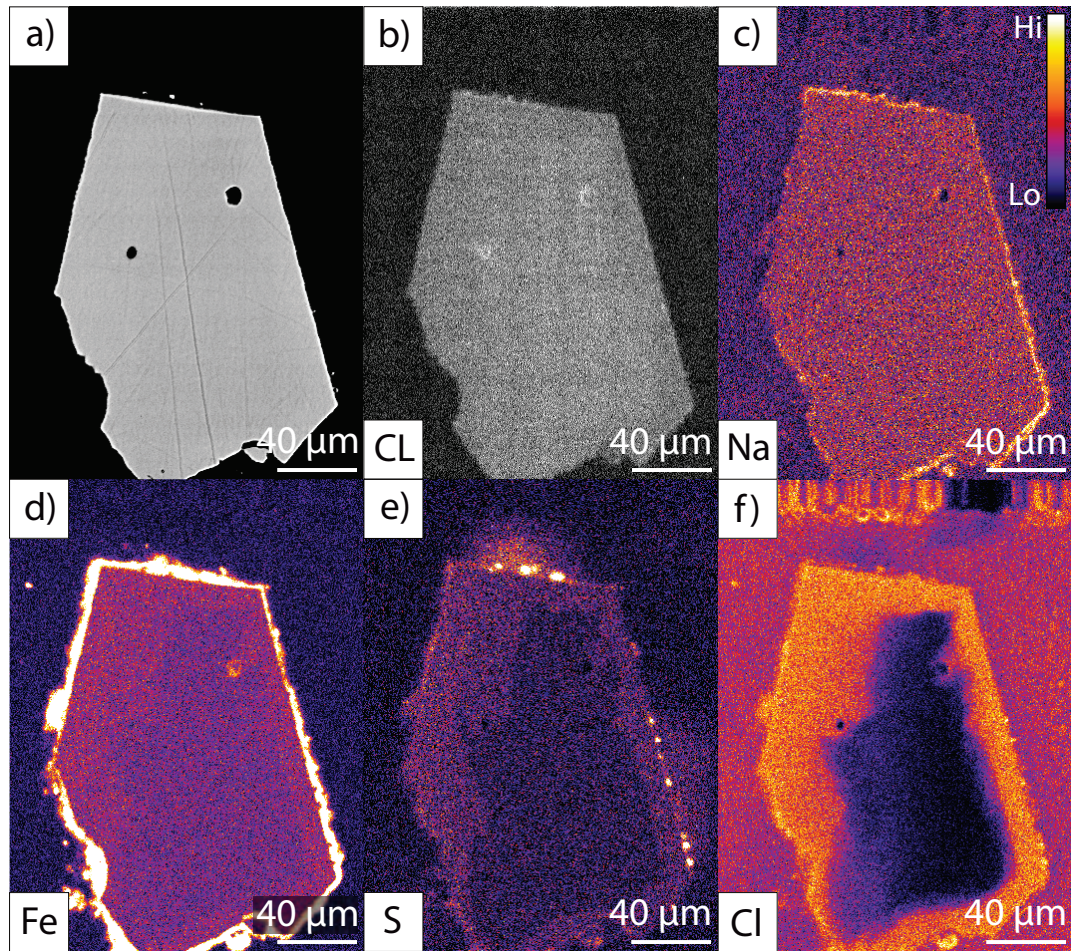


Figure 5

FS10: FIAp + 1M  $H_2SO_4$  +  $CeCl_3$  +  $CaCl_2$  +  $H_2O$

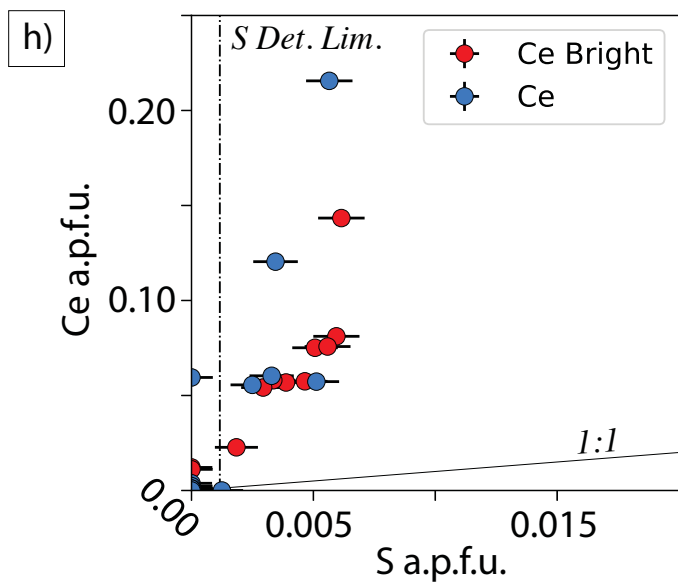
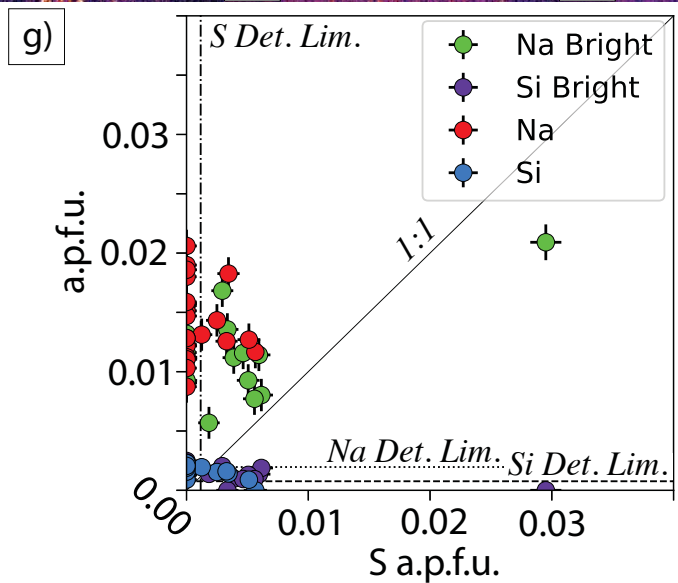
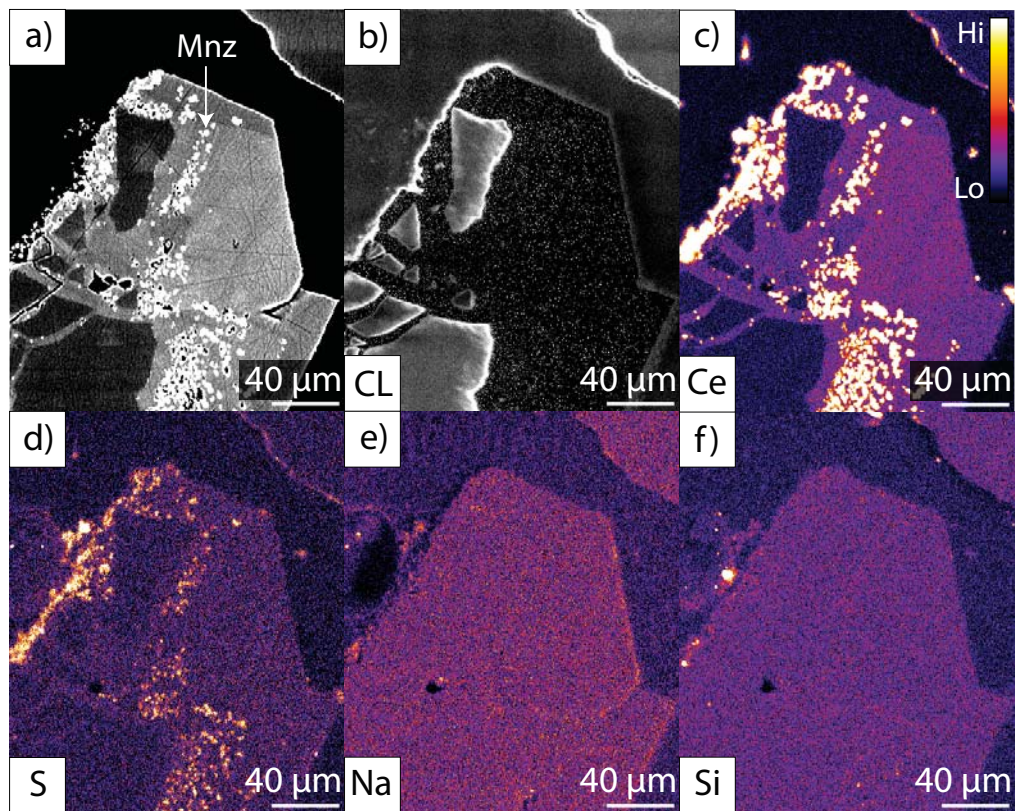




Figure 6

FS14: FIAP + Na<sub>2</sub>SO<sub>4</sub> + SrCl<sub>2</sub> + H<sub>2</sub>O

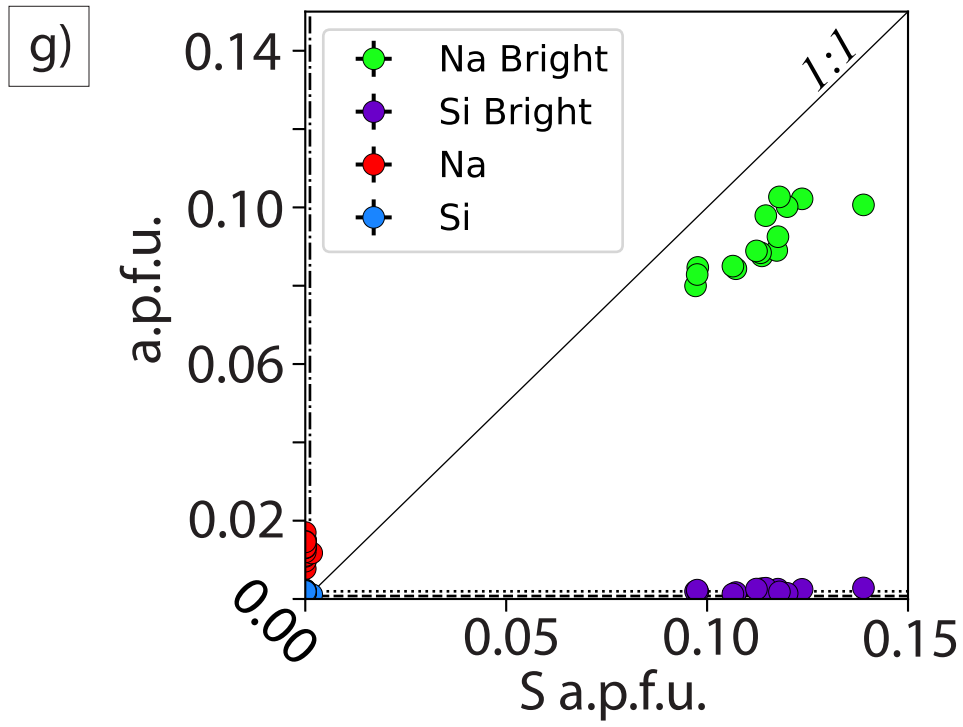
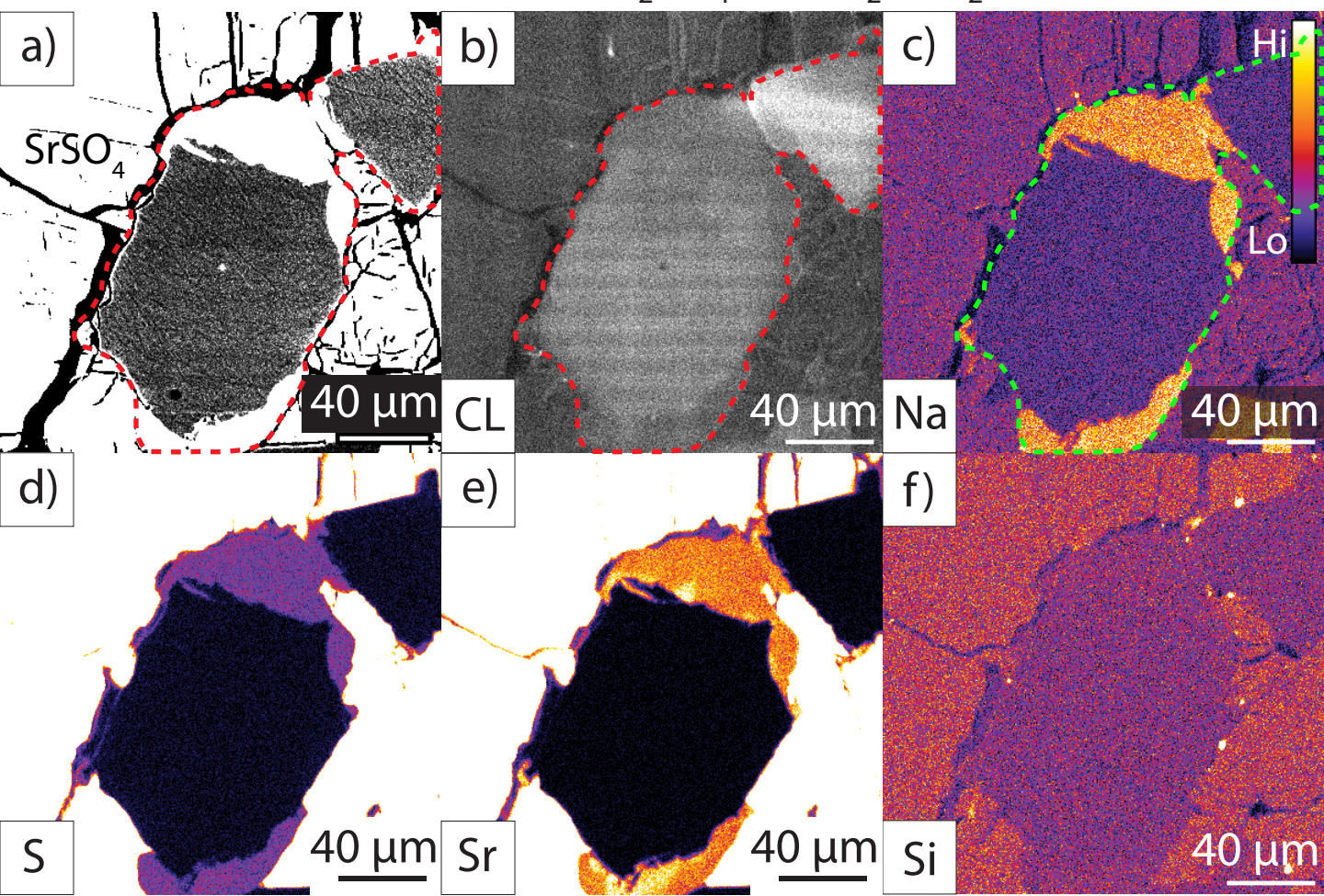




Figure 7

FS6-2: FIAP + FeS + H<sub>2</sub>O

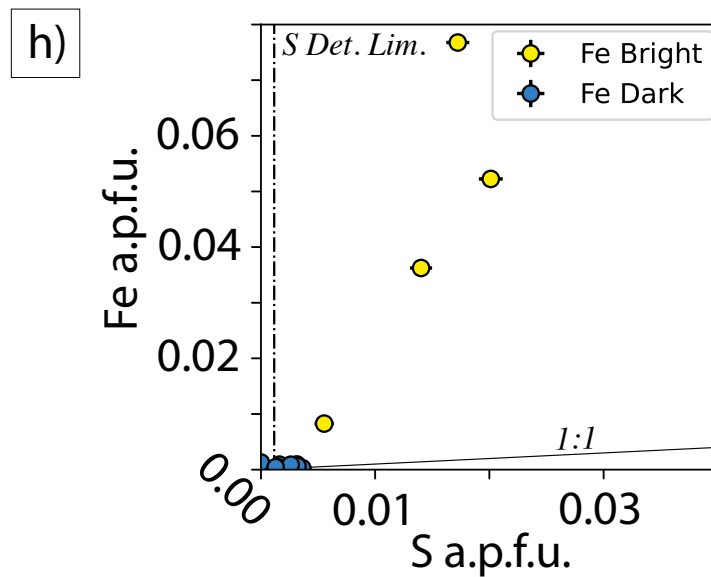
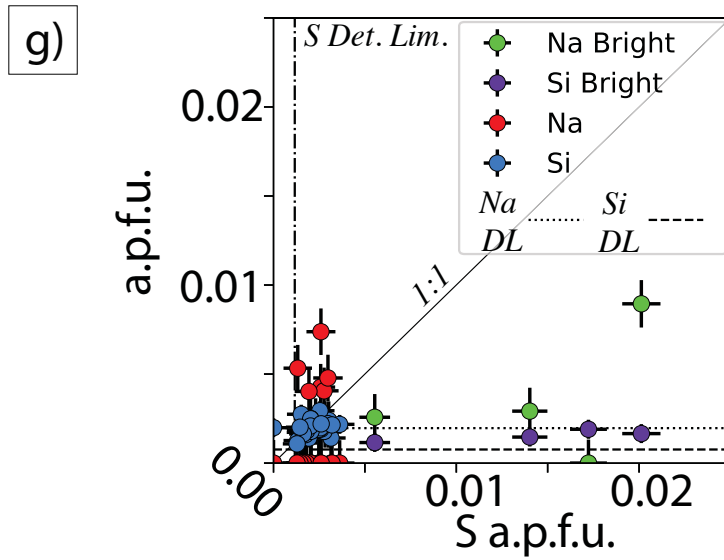
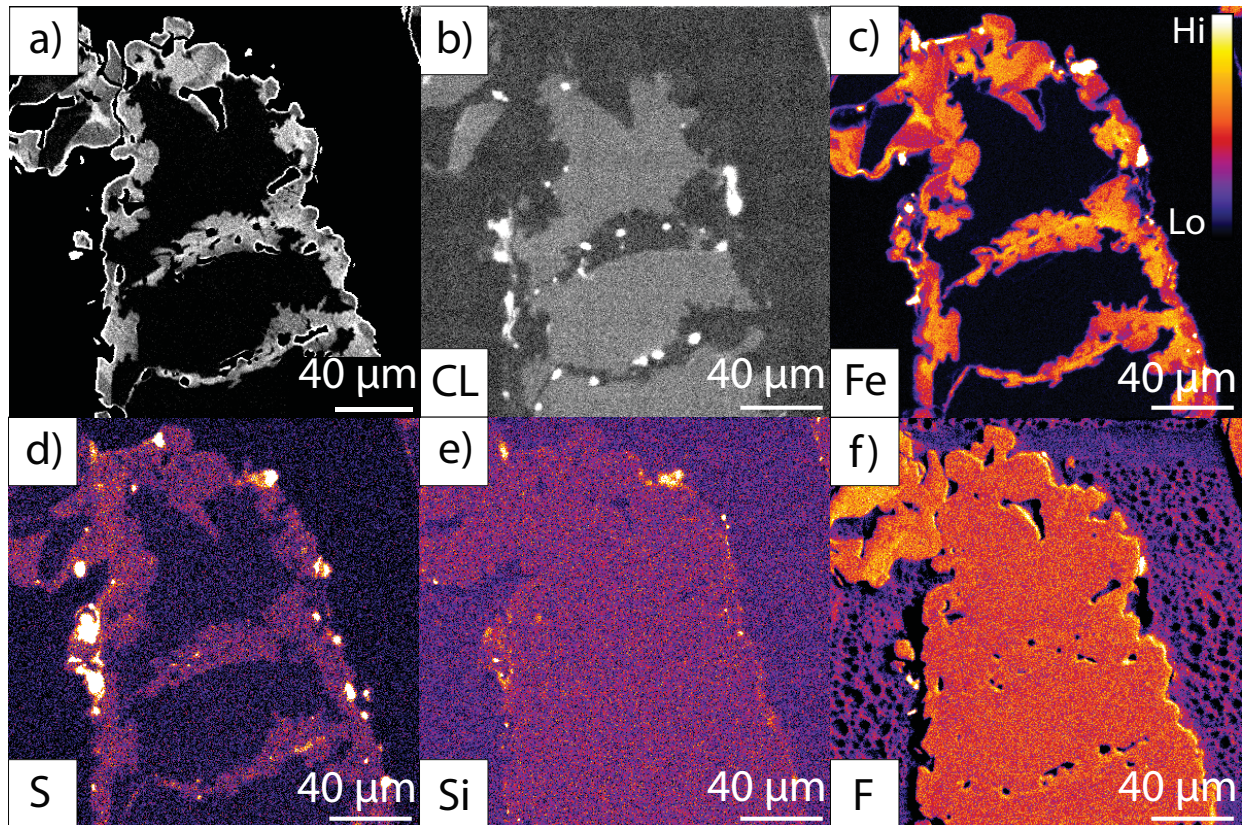


Figure 8

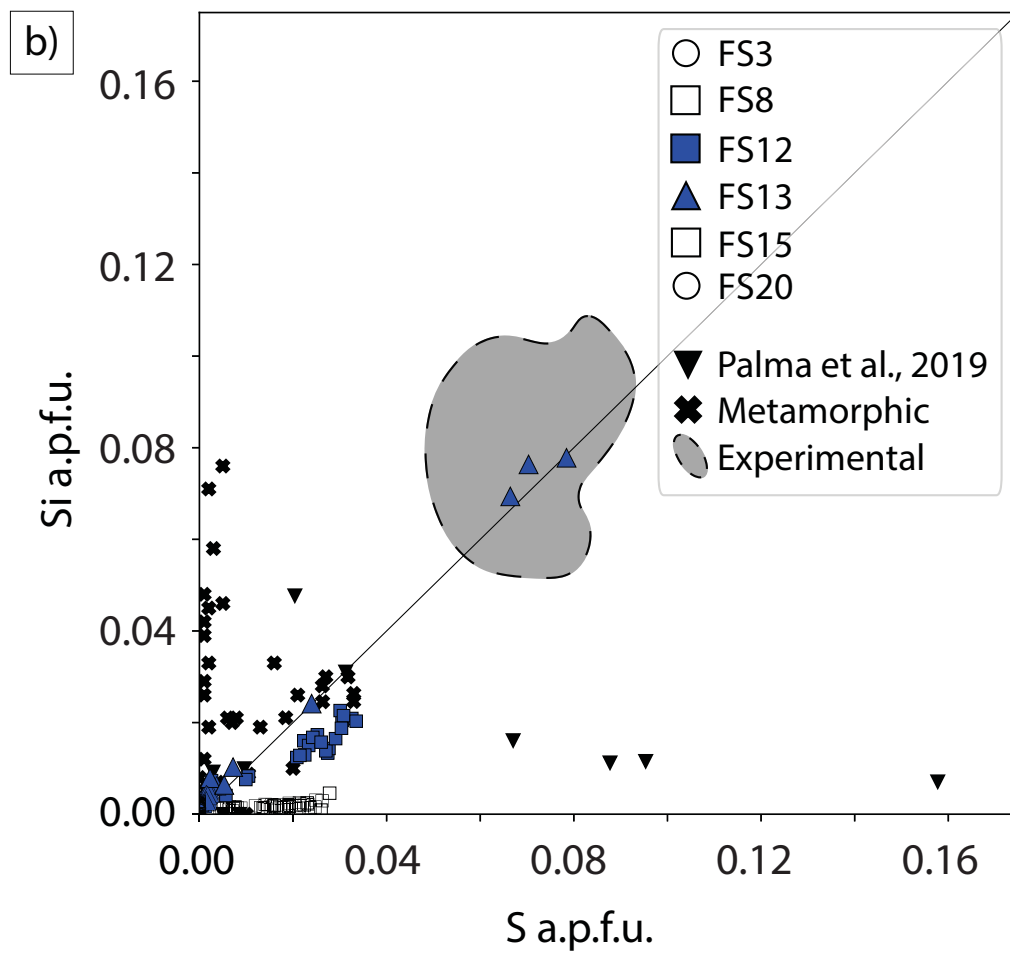
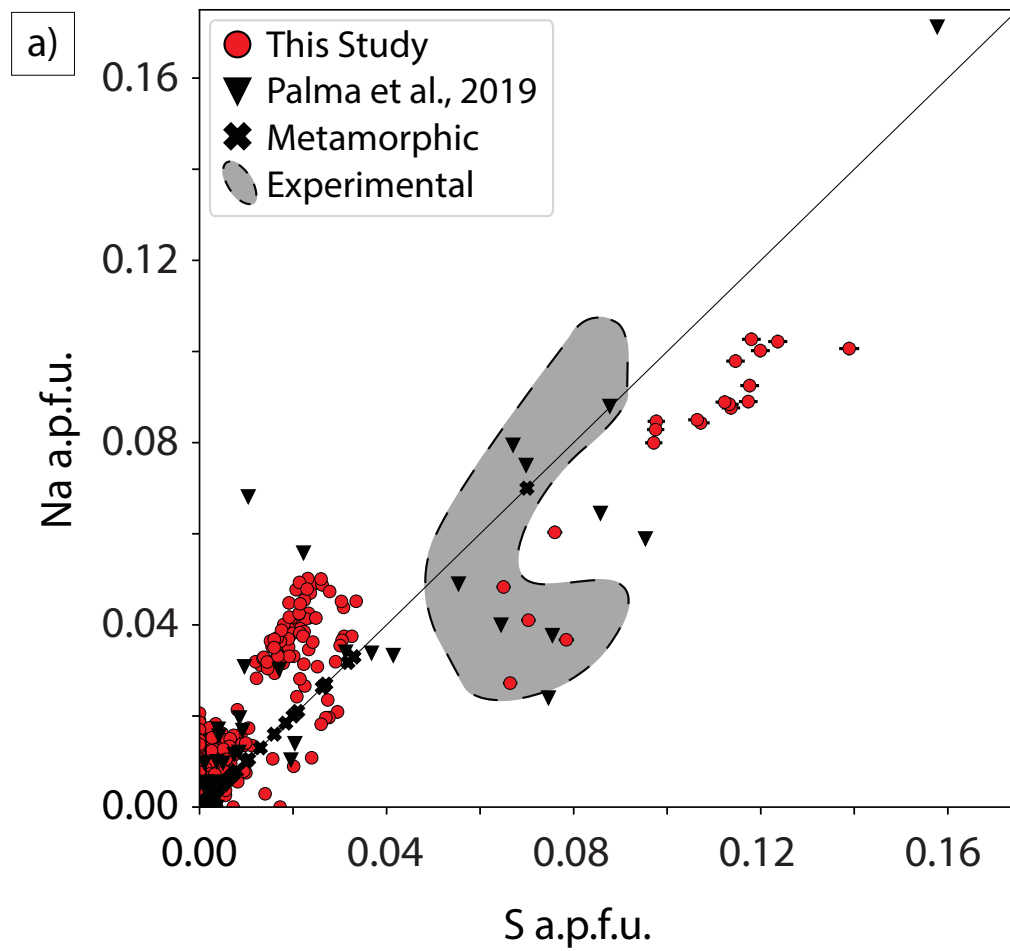


Figure 9

